Journal of Energy Chemistry 000 (2018) 1-23



Contents lists available at ScienceDirect

Journal of Energy Chemistry

journal homepage: www.elsevier.com/locate/jechem



http://www.journals.elsevier.com/ journal-of-energy-chemistry

Review

Cation engineering on lead iodide perovskites for stable and high-performance photovoltaic applications

Jue Gong^a, Peijun Guo^b, Savannah E. Benjamin^c, P. Gregory Van Patten^c, Richard D. Schaller^b, Tao Xu^{a,*}

- ^a Department of Chemistry and Biochemistry, Northern Illinois University, DeKalb, IL 60115, USA
- b Center for Nanoscale Materials, Argonne National Laboratory, 9700 South Cass Avenue, Lemont, IL 60439, USA
- ^c Department of Chemistry, Middle Tennessee State University, Murfreesboro, TN 37132, USA

ARTICLE INFO

Article history: Received 29 August 2017 Revised 27 November 2017 Accepted 2 December 2017 Available online xxx

Keywords:
Solar energy conversion
Perovskite solar cells
Power conversion efficiency
Optical bandgaps
Device hysteresis
Metastable phases

ABSTRACT

Perovskite solar cells (PSCs) based on methylammonium lead iodide (CH3NH3PbI3) have shown unprecedentedly outstanding performance in the recent years. Nevertheless, due to the weak interaction between polar CH₃NH₃+ (MA+) and inorganic PbI₃- sublattices, CH₃NH₃PbI₃ dramatically suffers from poor moisture stability, thermal decomposition and device hysteresis. As such, strong electrostatic interactions between cations and anionic frameworks are desired for synergistic improvements of the abovementioned issues. While replacements of I- with Br- and/or Cl- evidently widen optical bandgaps of perovskite materials, compositional modifications can solely be applied on cation components in order to preserve the broad absorption of solar spectrum. Herein, we review the current successful practices in achieving efficient, stable and minimally hysteretic PSCs with lead iodide perovskite systems that employ photoactive cesium lead iodide (CsPbI₃), formamidinium lead iodide (HC(NH₂)₂PbI₃, or FAPbI₃), $MA_{1-x-y-z}FA_xCs_yRb_zPbI_3$ mixed-cation settings as well as two-dimensional butylammonium ($C_4H_9NH_3^+$, or BA⁺)/MA⁺, polymeric ammonium (PEI⁺)/MA⁺ co-cation layered structures. Fundamental aspects behind the stabilization of perovskite phases α -CsPbI₃, α -FAPbI₃, mixed-cation MA_{1-x-y-z}FA_xCs_yRb_zPbI₃ and crystallographic alignment of (BA)₂(MA)₃Pb₄I₁₃ for effective light absorption and charge transport will be discussed. This review will contribute to the continuous development of photovoltaic technology based on PSCs.

© 2017 Science Press. Published by Elsevier B.V. All rights reserved.



Jue Gong received his B.S. in Chemistry (2013) from The University of Iowa, USA and is currently a senior Ph.D. student in Prof. Tao Xu's group at Northern Illinois University, USA. His research interests focus on photovoltaic studies of organic-inorganic hybrid perovskites.



Dr. Peijun Guo received his B.S. from Tsinghua University, China in 2009 and Ph.D. from Northwestern University, USA in 2016, both in Materials Science and Engineering. His research interests include optical studies of electronic and thermal processes of novel energy materials.



Savannah Benjamin is currently a senior undergraduate student at the Chemistry Department of Middle Tennessee State University under the guidance of Dr. Paul G. Van Patten. Her research direction is semiconductor quantum dots.

https://doi.org/10.1016/j.jechem.2017.12.005

2095-4956/© 2017 Science Press. Published by Elsevier B.V. All rights reserved.

^{*} Corresponding author. E-mail address: txu@niu.edu (T. Xu).



Paul G. Van Patten is the Chair of the Chemistry Department at Middle Tennessee State University, USA where his research focuses on semiconductor quantum dots. He received his B.A. in Chemistry (1992) from University of Virginia, USA and Ph.D. in Physical Chemistry (1996) from University of South Carolina, USA.



Richard D. Schaller is scientist at Center for Nanoscale Materials of Argonne National Laboratory, where his research focuses on laser spectroscopic investigations of electronic structures of quantum confined semiconductor materials. He received his B.A./M.S. in Chemistry (1997) from Northwestern University, USA and Ph.D. in Chemistry (2002) from University of California, Berkeley, USA.

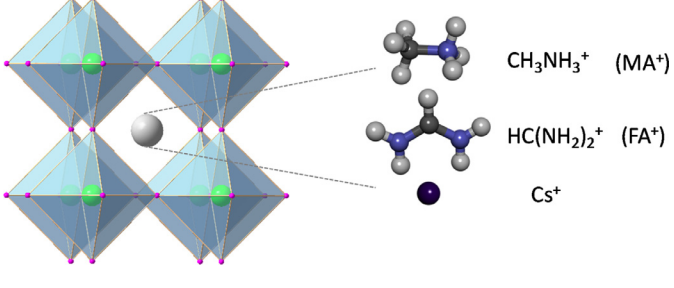


Fig. 1. Cubic perovskite structures of APbI₃ ($A = CH_3NH_3^+$, Cs^+ , $HC(NH_2)_2^+$). In the cubic APbI₃ perovskite structures, A-site cations, as represented by the gray sphere, are electrostatically intercalated in the interstitial voids formed by neighboring PbI₆ corner-sharing octahedral frameworks with minimal distortions (Pb-I-Pb angles at around 180°) [60,65,73,74], where Pb²⁺ and I⁻ are represented by green and pink spheres, respectively.



Tao Xu holds a tenured professorship at Department of Chemistry and Biochemistry of Northern Illinois University, USA where his research focuses on solid-state photovoltaics, fundamental optoelectronic mechanisms and ananomaterials for energy conversion and storage. He received his B.S. in Chemistry (1995) from East China University of Science and Technology and Ph.D. in Chemistry (2003) from University of Alabama, USA.

1. Introduction

Metal halide perovskites (MHPs, formula: ABX₃, A=Cs⁺, $CH_3NH_3^+$ (MA+) and/or $HC(NH_2)_2^+$ (FA+), $B=Pb^{2+}$ or Sn^{2+} , $C=I^-$, Br⁻ and/or Cl⁻) represent a realm of prominent light-harvesting active materials that have demonstrated unforeseen success in photovoltaic applications, where the record power conversion efficiency (PCE) of fabricated solar cells had rapidly risen from 3.8% in 2009 to 22.1% in 2016 [1,2]. The stunning realization of formidable photovoltaic performance was mostly achieved on solar cell devices with CH₃NH₃PbI₃ (MAPbI₃) being the photoactive layers [3–9]. Accordingly, what accounts for the outstanding performance of MAPbI₃ cells are its desirable material foundations, such as long carrier lifetimes (up to 3 ms), phenomenal charge carrier mobility (up to 60 cm 2 V $^{-1}$ s $^{-1}$) and long diffusion lengths (up to \sim 650 µm) [10–14]. From mechanistic standpoints, the superior carrier properties of MAPbI₃ stem from the easiness of free carrier generation due to small exciton binding energies (E_b , <10 meV) at ambient solar cell operation conditions [15–19], low trap-state densities of perovskite material ($\sim 10^9 - 10^{10}$ cm⁻³) [11], favored charge transport in three-dimensional (3-D) corner-sharing PbI₆ octahedral networks [20–22] that facilitate bond-to-bond electron hopping, as well as dynamic screening effects of MA⁺ on photocarriers via polaron formations that delay charge recombination [23–26]. Even though MAPbI₃ owns aforementioned attractive merits, it inherently suffers from poor moisture stability [27–33], where it decomposes to PbI2 due to solvation of MAI by moisture in the air [34-38]. Also, MAPbI₃ undergoes thermal degradation at elevated temperatures, in which volatile MAI separates from material lattice and causes significant loss of light-absorbing function of perovskite [39-43]. In terms of device operation, MAPbI₃ based solar cells are plagued by photocurrent density-voltage (J-V) hysteresis, where the J-V responses exhibit noticeable dependence on the directions, rates and even ranges of voltage scans [44-47], thereby making the accurate determination of power conversion efficiencies hard to realize. Importantly, the origins of J-V hysteresis are considered to be 1) capacitive current effects, 2) interfacial charge trapping and de-trapping, 3) dynamic band structure perturbations due to MA+/I-ion migration, as well as the induced built-in ferroelectric polarization [47]. By closely scrutinizing these problems, one can find that they all share the same root cause anisotropic MA⁺, which poses weak electrostatic interaction with anionic PbI₃- framework due to its localized cationic charge on NH₃⁺ group, and therefore is vulnerable to humidity solvation and thermal evaporation; meanwhile, mobile MA+ and its asymmetric geometry contribute to the polar nature of charge distribution in MAPbI₃ system, thus emphasizing the hysteretic effects. As such, it is imperative to strengthen the electrostatic attraction between A-site cations and lead iodide anionic frameworks, so as to enhance the stabilities and largely mitigate hysteresis behaviors of PSCs. Previously, various chemistry methods were applied to compositionally modify the lead iodide perovskites and achieved new material systems with significant moisture tolerance [48–50]. For example, pseudohalide SCN- was used to partially substitute I- in perovskite lattice to passivate the solvation of MA+ under moisture effects [48,49]. Nevertheless, this approach inevitably resulted in Ruddlesden-Popper type two-dimensional (2-D) (MA)₂Pb(SCN)₂I₂ perovskite [51]. Such material and analogous 2-D perovskites confine charge transport within inorganic layers, and lead to largely widened optical bandgaps that consequently narrow the optical absorption range of solar spectrum, thus limiting the photovoltaic performance of fabricated solar cell devices [52-56]. In addition, 2-D lead iodide perovskites are reported to have even weaker thermal stabilities, when compared with their 3-D MAPbI₃ counterpart [57]. Likewise, although greater stabilities of perovskite materials were achieved by partially replacing I- with Br- or Cl-, their optical bandgaps were concomitantly widened, and therefore led to decreased photocurrents of fabricated devices [9,22,58,59]. To date, there is no synergistic approach to mitigate the issues of poor moisture stabilities, thermal degradations and device hysteresis, while simultaneously preserving the optical absorption efficiency on lead iodide perovskites from the anion perspective. Being a monovalent cation with isotropic charge distribution, Cs⁺ has the potential to stabilize lead iodide perovskites by forming stronger, and more homogeneous electrostatic attraction with the inorganic PbI_3 frameworks. Previously, as shown in Fig. 1, α -phase cubic perovskite CsPbI₃ was found to have a similar crystal structure and optical bandgap with α -MAPbI₃ (1.73 eV; MAPbI₃: 1.53 eV) [59–61], thereby signifying the feasibility of a photo-absorber that can be used to replace unstable MAPbI₃ counterpart. Nonetheless, its photoactive black phase was thermodynamically unstable below \sim 320 °C [60-65], thereby making the pristine form still hard to realize. Similarly, FA+ resembles a charge-delocalized cation

2

that has led to moisture– and thermally stable cubic perovskite FAPbI $_3$ (α -FAPbI $_3$, structure illustrated in Fig. 1) with narrower material bandgaps (1.4 eV–1.5 eV) and remarkable photovoltaic properties [66–68]. However, α -FAPbI $_3$ is also unstable at ambient temperatures, where it converts to non-perovskite yellow phase [60,63,68–72]. Therefore, it is fundamentally intriguing to seek special measures to coherently tune the interplay between cations and lead iodide sublattices, for generating greater structural allowance (e.g. Goldschmidt tolerance factors) while retaining exceptional absorption/carrier properties.

Here, we systematically review the recent successful methods in stabilizing pure Cs+ and FA+ based lead iodide perovskites, as well as $MA_{1-x-y-z}FA_xCs_yRb_zPbI_3$ mixed-cation systems for stable and efficient PSCs. Additionally, novel practices of adopting homologous alkylammoniums and polymeric ammoniums in 2-D iodide systems to achieve phenomenal solar cell performance will also be analyzed. In the end, future research directions of MHPs are to be discussed. This work could provide insightful guidelines in furthering the improvements of MHPs in both material and photovoltaic settings.

2. Perovskites α -CsPbI₃ and β -CsPbI₃

2.1. Stabilization of perovskite phase $\alpha\text{-CsPbI}_3$

2.1.1. Characterization of α -CsPbI₃ quantum dots

Due to the small size of Cs⁺ (r = 167 pm; MA⁺: 270 pm) [75], CsPbI₃ unavoidably has a small resultant Goldschmidt tolerance factor, which is defined as: $t = (r_A + r_X)/(2^{1/2} * (r_B + r_X))$, where r_A , r_B and r_X represent the radii of A-, B- and X-site ions, respectively [63,76,77]. While a t value between 0.9 and 1.0 indicates an optimal cubic perovskite structure, CsPbI $_3$ has a t smaller than 0.8, thereby forming non-perovskite phase under ambient conditions [63,76]. It was previously shown by Swarnkar et al. [61] that α -CsPbI₃ can be stabilized in the form of quantum dots (QDs). α -CsPbI₃ QDs were first synthesized by introducing Cs-oleate solution at temperatures ranging from 60 °C to 185 °C to PbI2 in containers; as-formed QDs were chelated by oleylammonium (OA+) surface ligands [61]. Prepared α -CsPbI₃ QDs were washed with methyl acetate to remove excess precursors without coalescence [61]. Purified α -CsPbI₃ QDs displayed tunable optical absorption and emission properties due to varied bandgaps and associated particle sizes. As shown in Fig. 2(a), UV-visible absorption onset of CsPbI₃ QDs redshifts as synthesis temperature elevates, thus indicating a narrower bandgap at higher temperature. This is echoed with UV-excited photoluminescence (PL) of CsPbI₃ QDs, where QDs synthesized at higher temperature correspond to PL emission with greater peak wavelength, as shown in Fig. 2(b). As such, it can be inferred that higher temperatures led to CsPbI₃ QDs with larger sizes. As shown in Fig. 2(c), high-resolution TEM image indicates that CsPbI₃ QDs synthesized from 180 °C condition was in around 10 nm of size, which was monotonically greater than QDs prepared at 170 °C, 150 °C, 130 °C, 100 °C and 60 °C that have 8 nm, 6.8 nm, 5 nm, 4.5 nm and 3.4 nm of sizes, respectively [61]. Importantly, cubic nature of synthesized CsPbI3 QDs was confirmed by the Xray diffraction (XRD) patterns, as shown in Fig. 2(d), where QDs synthesized from 60 °C to 185 °C all shared diffraction peaks at around 14°, 20°, 24° 28°, 32°, 35°, 41°, 43° and 46° which are characteristic to cubic structure, thereby proving the desirable α -CsPbI₃ phase.

2.1.2. Photovoltaic properties of α -CsPbI $_3$ QDs

Photocurrent–voltage (J–V) measurements were conducted to examine the photovoltaic performance of α -CsPbI $_3$ QDs based solar cell device [61]. As shown in Fig. 3(a) and (b), α -CsPbI $_3$ QDs

based device adopted a planar solar cell architecture with TiO2 being the electron transport layer and spiro-OMeTAD being the hole transport layer [78–85]. Specifically, MoO_x/Al structure was used as hole-collecting photoanode, which was low-cost and proved to promote hole extraction due to the oxygen-deficient nature of molybdenum oxide; also, MoO_x/Al composite electrodes effectively suppressed perovskite degradation under ambient conditions and enhance device stability, as reported by other works [86-89]. As shown in Fig. 3(c), α -CsPbI₃ QDs based cell exhibits short-circuit current density (J_{sc}) as ~12.9 mA cm⁻² and open-circuit voltage $(V_{\rm oc})$ as \sim 1.15 V within the first day of fabrication (magenta curve); after 9 days of aging in ambient air, device showed nearly unchanged J_{sc} but increased V_{oc} to $\sim 1.23 \, \text{V}$ (orange curve). Top PCE was achieved as 10.77% with $V_{\rm oc}$ being 1.23 V, $J_{\rm sc}$ being 13.47 mA cm⁻² and fill factor (FF) as 0.650, 15 days after first fabrication (black curve). The progressive improvement of photovoltaic characteristics illustrates the outstanding stability and performance of α -CsPbI₃ QDs based solar cell.

2.1.3. Zwitterion-stabilized α -CsPbI $_3$ for stable and efficient photovoltaic performance

Other than OA+ ligand, Wang and coworkers [90] demonstrated that sulfobetaine zwitterions could also be utilized to stabilize α -CsPbI₃ so as to form small-grain perovskite thin films, where the chemical structures of three adopted sulfobetaine zwitterions are shown in Fig. 4(a). As shown in Fig. 4(b), with the presence of one zwitterion-NDSB201, stabilized film displayed a broad light absorption from 350 nm to greater than 700 nm, in contrast to assynthesized CsPbI₃ that only absorbed up to ~600 nm. The large coverage of solar spectrum by NDSB201-stabilized thin film thus had a strong black color, as shown in Fig. 4(c); and its optical bandgap (\sim 1.74 eV), as indicated by \sim 710 nm PL peak wavelength in Fig. 4(d), directly evidenced the formation of photoactive α -CsPbI₃ phase. As shown in Fig. 4(e), the cubic phase of stabilized perovskite α -CsPbI $_3$ was further verified by XRD patterns, where perovskite (001), (011) and (002) planes are unambiguously present, and is agreeing well with previous reports [61,65,91,92]. Moreover, the NDSB201-induced α -CsPbI₃ thin film exhibit a long-term stability in the air for 60 days, as seen from the nearly unchanged diffraction pattern (Fig. 4e bottom). Most importantly, by adopting an inverted solar cell structure (p-i-n, Fig. 4f), where poly[bis(4-phenyl)(2,4,6-trimethylphenyl)amine] (PTAA) was used as p-type hole transport layer and [6,6]-phenyl C61 butyric acid methyl ester (PCBM), C₆₀ and 2,9-dimethyl-4,7-diphenyl-1,10phenanthroline (BCP) were used as n-type electron transport layers [20,32,66,90,93,94], a top PCE of 11.4% was achieved on zwitterionstabilized film along with a V_{oc} , J_{sc} and FF as 1.08 V, 14.9 mA cm⁻² and 0.7, respectively (Fig. 4g). Also, as shown in Fig. 4(h), unencapsulated device based on zwitterion-stabilized film displayed a ~9% PCE after 35 days of aging in air under dark condition, which accounted for a retention that was nearly 80% of original solar cell performance.

2.2. Phase retention and photovoltaic application of perovskite β -CsPbI $_3$

As inspired by the intermediate β -phase perovskites CsSnI₃ and CsPbBr₃ [95–97], Fu et al. previously hypothesized and confirmed the existence of photoactive β -CsPbI₃, which is in orthorhombic structure [98]. It is worth mentioning that δ , β and α phases respectively represent materials with increasing symmetries and thermodynamic temperatures, with δ -phase completely losing the 3-D corner-sharing octahedral network and thereby signifying non-perovskite crystal structure [60]. However, β -phase materials maintain the structural characteristics of perovskites that are featured with distorted inorganic octahedra (bent B-X-B bonds)

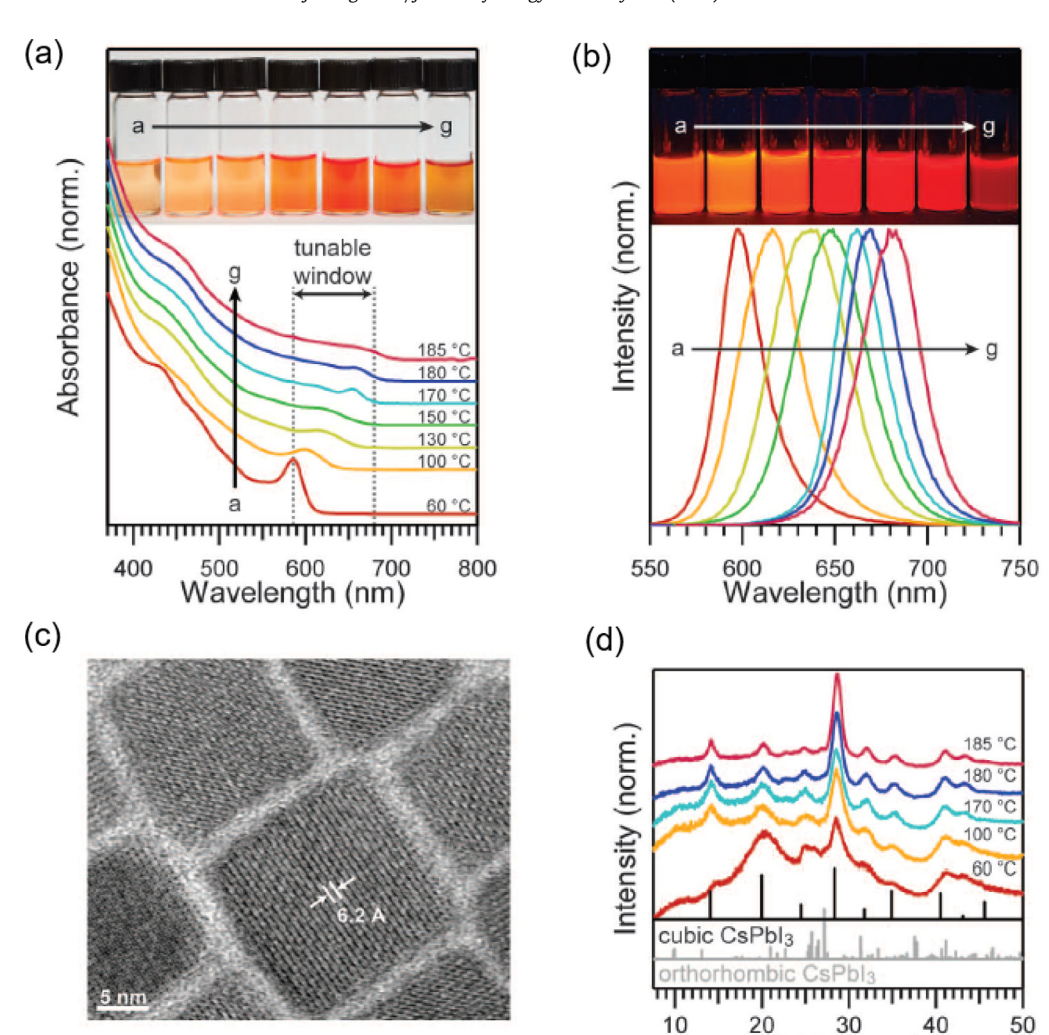


Fig. 2. Optical and structural characterization of α -CsPbl₃ QDs [61]. (a) Photographs and corresponding UV-vis absorption spectra of α -CsPbl₃ QDs synthesized at 60 °C, 100 °C, 150 °C, 150 °C, 150 °C, 150 °C, 180 °C and 185 °C, as labeled from a to g. (b) Photographs of the α -CsPbl₃ QDs shown in (a) under UV illumination and corresponding PL spectra. (c) High-resolution TEM image of α -CsPbl₃ QDs prepared at 180 °C with lattice parameter equal to around 6.2 Å. (d) XRD patterns of α -CsPbl₃ QDs prepared at 60 °C (red), 100 °C (yellow), 170 °C (light-blue), 180 °C (blue), 185 °C (pink), calculated cubic α -CsPbl₃ (black) and calculated orthorhombic phase δ -CsPbl₃ (gray). © American Association for the Advancement of Science (AAAS). Reprint by permission of AAAS from ref. [61]. Permission to reuse must be obtained from the copyright holder.

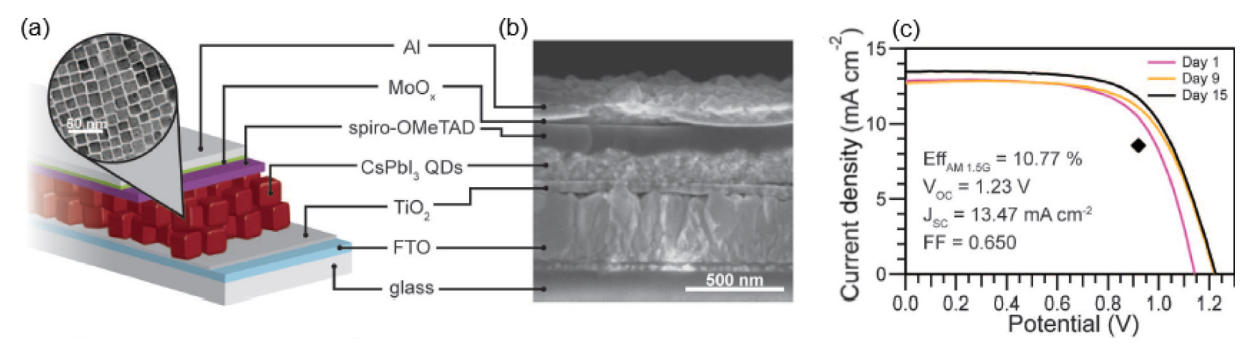


Fig. 3. Photovoltaic properties of α -CsPbl₃ QDs based solar cell [61]. (a) Architecture of α -CsPbl₃ QDs based solar cell device. (b) Cross-section scanning electron microscopy (SEM) image of fabricated device, displaying each individual layer. (c) J–V curves of α -CsPbl₃ QDs based device (day 1: magenta; day 9: yellow; day 15: black) with calculated photovoltaic parameters. © AAAS. Reprint by permission of AAAS from ref. [61]. Permission to reuse must be obtained from the copyright holder.

[99], and are therefore of great exploitation in photovoltaics. Interestingly, Fu and coworkers demonstrated that phenylethylammonium ($C_6H_5(CH_2)_2NH_3^+$, PEA⁺) could stabilize metastable β -CsPbI₃ perovskite during one-step thin film deposition, while OA⁺ surface ligand stabilized CsPbI₃ in cubic α -phase and the lack of long-chain ammonium ligand directly resulted in yellow δ -CsPbI₃; and structures of ligand additives and polymorphic CsPbI₃ are

4

shown in Fig. 5(a), (b) and (c). The perovskite structure of orthorhombic β -CsPbI₃, as stabilized by PEA⁺ ligand, was confirmed by the doublet (200) peak at around 28° of corresponding XRD pattern (blue) that is shown in Fig. 5(d), while OA⁺ functionalized thin film showed a cubic structure as manifested in singlet peaks of (100), (200) planes that are at around 14°, 28°, respectively (red pattern). Without surface ligand, as-formed thin

2θ (degrees)

Please cite this article as: J. Gong et al., Cation engineering on lead iodide perovskites for stable and high-performance photovoltaic applications, Journal of Energy Chemistry (2018), https://doi.org/10.1016/j.jechem.2017.12.005

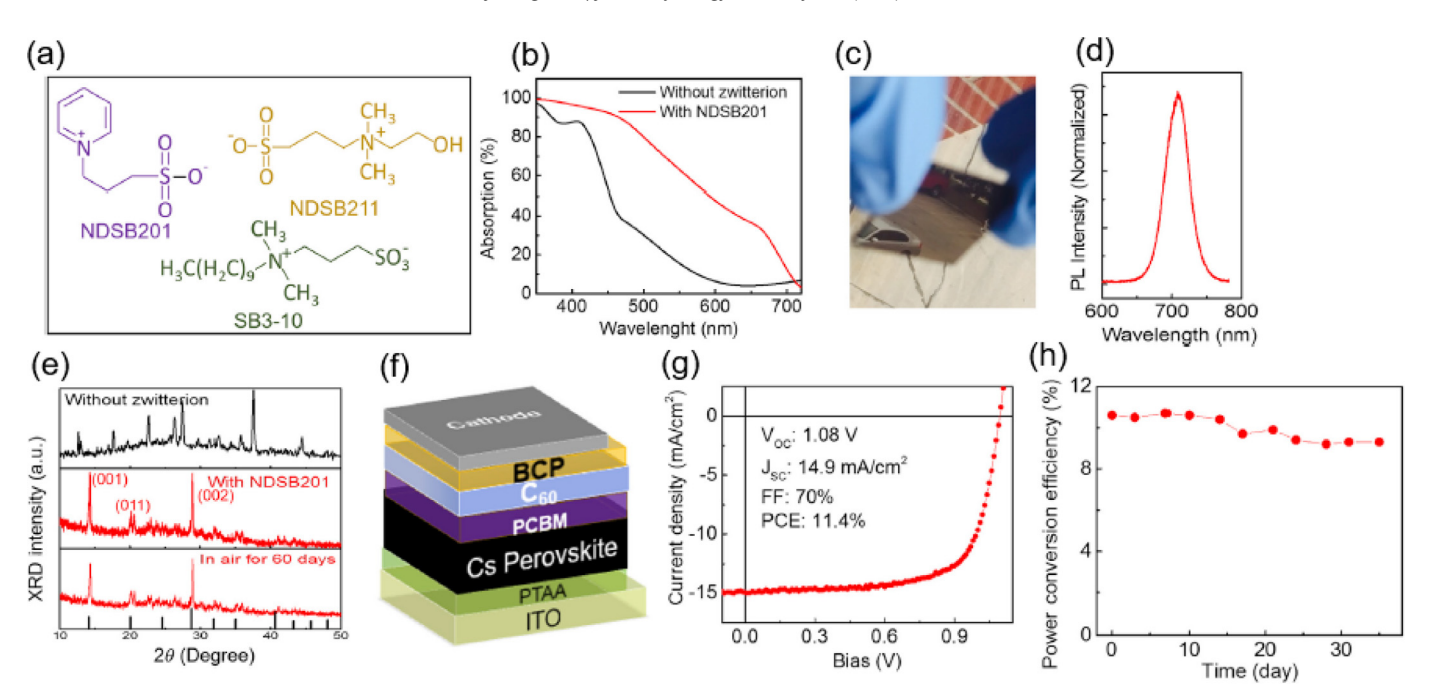


Fig. 4. Structural, optical and photovoltaic properties of CsPbl₃ films [90]. (a) Chemical structures of three sulfobetaine zwitterions used in stabilizing α -CsPbl₃. (b) UV-vis absorption of δ-CsPbl₃ thin film without zwitterion additive (black) and NDSB201-stabilized α -CsPbl₃ thin film (red). (c) Photograph of a black and reflective zwitterion-stabilized α -CsPbl₃ thin film. (d) PL spectrum of zwitterion-stabilized α -CsPbl₃ thin film. (e) Comparison of XRD patterns of δ-CsPbl₃ film without zwitterion additive (black), α -CsPbl₃ film stabilized by NDSB201 before (middle) and after storage in air for 60 days (bottom) at room temperature under dark condition. (f, g) Architecture, J-V curve of zwitterion-stabilized α -CsPbl₃ based solar cell, respectively. (h) Stability test of PCE of unencapsulated α -CsPbl₃ based solar cell across 35 days of aging in ambient air under dark condition. © Cell Press. Reproduced with permission granted by Cell Press from ref. [90]. Permission to reprint must be obtained from the copyright holder.

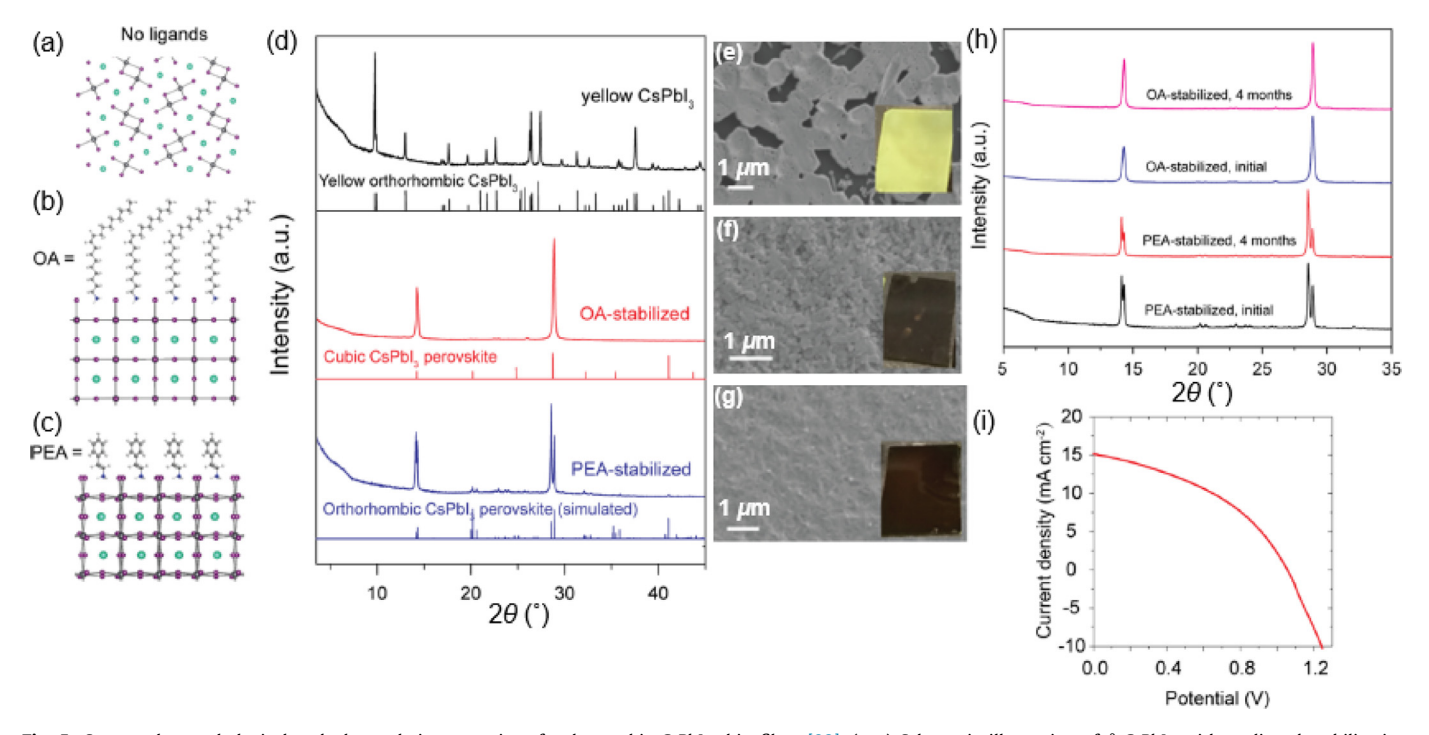


Fig. 5. Structural, morphological and photovoltaic properties of polymorphic CsPbI₃ thin films [98]. (a–c) Schematic illustration of δ -CsPbI₃ without ligand stabilization, α -CsPbI₃ with OA⁺ functionalization, β -CsPbI₃ with PEA⁺ functionalization, respectively. (d) Corresponding XRD patterns with or without surface ligand stabilization. (e–g) Corresponding SEM images of CsPbI₃ thin film surfaces, with inset being photographs of thin films. (h) Comparison of XRD patterns of OA⁺-stabilized α -CsPbI₃, PEA⁺-stabilized β -CsPbI₃ across 4 months of aging in the air at room temperature. (i) J–V curve of PEA⁺-stabilized β -CsPbI₃ solar cell. © American Chemical Society (ACS). Reproduced with permission granted by ACS from ref. [98]. Permission to reuse must be obtained from the copyright holder.

film also displayed an orthorhombic structure, but in the absence of perovskite (100) and (200) structures (black pattern). δ -phase, β -phase and α -phase CsPbI₃ polymorphs were further corroborated with photographs that correspondingly show yellow, black and brown colors of respective thin films in Fig. 5(e), (f) and (g). Furthermore, ligand-functionalized CsPbI₃ exhibited long-term sta-

bility that is up to 4 months in the air at room temperature, as indicated by XRD patterns in Fig. 5(h). Eventually, as shown in Fig. 5(i), PEA⁺-stabilized β -CsPbI₃ solar cell showed a considerable photovoltaic performance with 6.5% PCE that was characteristic of 15.0 mA cm⁻², 1.06 V and 0.41 as $J_{\rm sc}$, $V_{\rm oc}$ and FF, respectively.



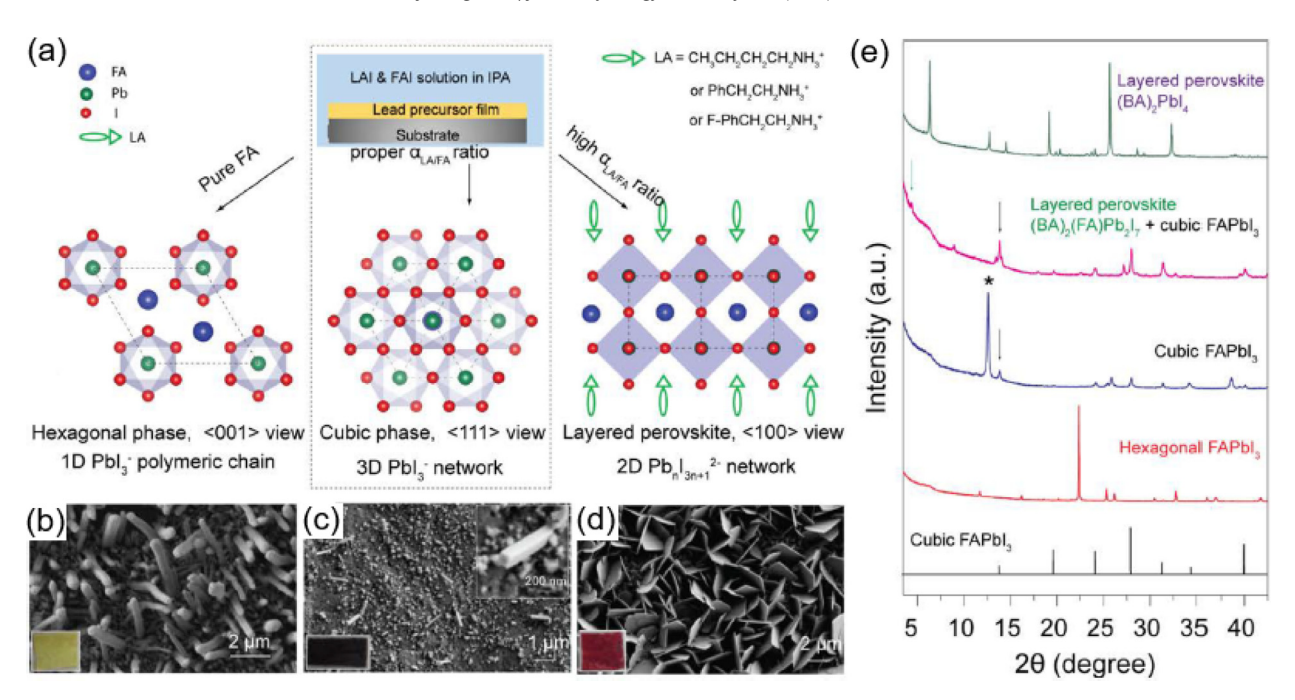


Fig. 6. Morphological and structural characterizations of synthesized formamidinium lead iodide materials [101]. (a) Schematic illustration and crystal structures of solution-grown δ -FAPbl₃, α -FAPbl₃ and (LA)₂(FA)Pb₂l₇, (b–d) SEM images of as-synthesized δ -FAPbl₃, α -FAPbl₃ and (BA)₂(FA)Pb₂l₇, respectively, with insets being the respective photographs of as-synthesized thin films. (e) Powder XRD patterns of as-grown hexagonal δ -FAPbl₃ (red), cubic α -FAPbl₃ (blue, with "*" indicating Pbl₂), layered (BA)₂(FA)Pb₂l₇ perovskite mixed with cubic α -FAPbl₃ (magenta, with arrow indicating the α -FAPbl₃ structure), pristine (BA)₂Pbl₄ (green) and calculated cubic α -FAPbl₃ pattern (black). © ACS. Reproduced with permission granted by ACS from ref. [101]. Permission to reuse must be obtained from the copyright holder.

3. Perovskite α -FAPbI₃

3.1. Stabilization of perovskite phase α -FAPbI₃

In contrast to the small size of Cs+, FA+ has larger ionic radii as 279 pm, and it directly leads to Goldschmidt tolerance factor greater than 1 at ambient conditions, which is responsible for the detrimental phase transition from black cubic α -FAPbI $_3$ to yellow non-perovskite hexagonal δ -FAPbI $_3$ at room temperature (RT) [63,75,100]. Hence, it is of great intrigue to stabilize the photoactive α -FAPbI $_3$ phase to harness its remarkable photovoltaic properties over long-term solar cell operations.

3.1.1. Morphological and structural characterization of formamidinium lead iodide compounds synthesized w/ or w/o BA $^+$

It was previously reported by Fu and coworkers that long-chain alkyl and aromatic ammonium ligands (denoted as LA+) can stabilize the solution-grown α -FAPbI₃ nanocrystal thin films, without involving high temperature (HT) conversion from δ -FAPbI $_3$ to cubic α -FAPbI₃ phase [101]. As shown in Fig. 6(a), PbI₂ or Pb(CH₃COO)₂ was first deposited on TiO2 coated FTO glass; lead precursor film was then dipped into iodide salt/isopropanol solutions that comprise LAI and FAI in various molar ratios for developing different nanostructures, where LA⁺ can be CH₃CH₂CH₂CH₂NH₃⁺ (BA⁺), PEA⁺ or F-PhCH₂CH₂NH₃⁺ (4-fluorophenylethylammonium, or FPEA⁺). When no LAI was present in precursor solution $(\alpha_{\text{LA/FA}} = 0)$, δ -FAPbI₃ was always formed upon the reaction between PbI₂ and FAI, with the surface morphology of as-fabricated film showing one-dimensional nanowires in micrometer lengths, as shown in Fig. 6(b), and its XRD pattern was shown in red of Fig. 6(e) [101]. The identity of hexagonal δ -FAPbI₃ is evidenced by the yellow color of as-fabricated film displayed in Fig. 6(b) inset. However, when BA $^+$ was used as the ligand with $\alpha_{\rm BA/FA}$ adjusted to be 0.86, as-converted film shows significantly decreased 1-D nanostructures and a black color, as shown in Fig. 6(c) and inset, respectively, thereby indicating generation of a photoactive material with higher structural dimension. The cubic structure of α -FAPbI₃ was confirmed by XRD as shown in blue of Fig. 6(e), showing some unreacted PbI₂. After $\alpha_{BA/FA}$ increased to 2.57, plate-like 2-D layered structures were formed, as shown in Fig. 6(d), where the materials were found to be the mixture of cubic α -FAPbI₃ and 2-D (BA)₂(FA)Pb₂I₇, as verified by magenta pattern of Fig. 6(e). The red color of inset photograph of as-fabricated film illustrated a widened bandgap of 2-D perovskite due to quantum confinements, when compared with the 3-D α -FAPbI₃ counterpart. As BA⁺ content continuously increased in BAI/FAI precursor solution, pure (BA)₂PbI₄ was formed, as shown in green of Fig. 6(e) [101].

3.1.2. PEA^+ -, $FPEA^+$ -stabilized and photovoltaic properties of α -FAPhl₂

The surface functionalization by PEA+ and FPEA+ also led to stabilized cubic phase α -FAPbI₃ [101]. As shown in Fig. 7(a), XRD patterns indicate nearly identical perovskite structures of α -FAPbI₃ nanostructures stabilized by FPEA+ (green), PEA+ (light blue) and BA+ (red) by peaks at around 14°, 20°, 24°, 28°, 31°, 35° and 40°, when compared to calculated pattern of cubic phase FAPbI₃ (black). Remarkably, as shown in Fig. 7(b), α -FAPbI₃ thin film functionalized with FPEA+ preserved cubic structure that did not experience noticeable change in diffraction pattern over 4 months of aging, which is corroborated by the black color of α -FAPbI₃ thin film displayed as inset. PL studies were performed to validate the photoactive cubic phase of LA-directed formation of α -FAPbI₃. As shown in Fig. 7(c), BA+- (black), PEA+- (pink), FPEA+-(blue) stabilized and δ - α thermally transitioned (magenta) FAPbI₃ all shared a common emission peak wavelength at around 814 nm that corresponds to a \sim 1.50 eV bandgap and agrees well with previous reports [67,76,100,102], thus verifying the cubic phase α -FAPbI₃. Most importantly, the photovoltaic properties of FPEA⁺stabilized α -FAPbI $_3$ were studied by conducting J-V measurements of fabricated solar cell device. As shown in Fig. 7(d), stabilized α -FAPbI₃ device (red) exhibited better photovoltaic performance

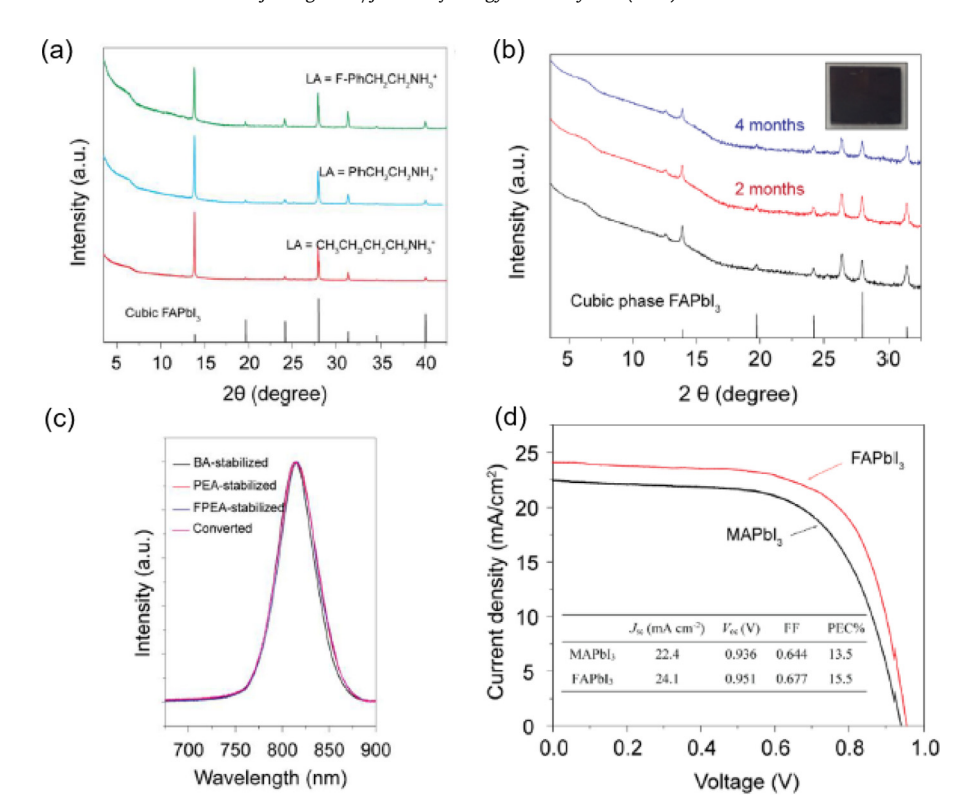


Fig. 7. Structural, optoelectronic and photovoltaic properties of ligand-stabilized α -FAPbl₃ [101]. (a) XRD patterns of perovskite FAPbl₃ nanostructures prepared from Pbl₂ films in FAI/BAI (red), FAI/PEAI (blue) and FAI/FPEAI precursor solutions, indicating the formation of cubic structures by comparing with calculated cubic α -FAPbl₃ pattern (black). (b) Evolution of XRD patterns of α -FAPbl₃ nanocrystal film converted from Pbl₂ and FAI/FPEAI precursors, with as-fabricated film, 2 months and 4 months of aging shown in black, red and blue, respectively. The high stability of synthesized α -FAPbl₃ film was indicated by the nearly unchanged cubic structure by comparing to calculated cubic α -FAPbl₃ pattern (bottom), and by the black film shown as inset photograph. (c) PL spectra of α -FAPbl₃ converted from δ-FAPbl₃ through thermal treatment (magenta), Pbl₂ in FAI/FPEAI solution (blue), Pbl₂ in FAI/PEAI (pink) and Pbl₂ in FAI/BAI solution (black). Overlapped spectra illustrated a conformed cubic structure across all ligand-stabilized α -FAPbl₃ with a same bandgap. (d) J-V curves of α -FAPbl₃ based solar cell (red) as fabricated from FAI/FPEAI solution and MAPbl₃ based device (black), with inset showing extracted photovoltaic parameters from corresponding devices. © ACS. Reproduced with permission granted by ACS from ref. [101]. Permission to reprint must be obtained from the copyright holder.

as relative to a reference MAPbI₃ device (black) with greater J_{sc} (24.1 mA cm⁻²; MAPbI₃: 22.4 mA cm⁻²) and V_{oc} (0.951 V; MAPbI₃: 0.936 V); in addition, stabilized α -FAPbI₃ device had a larger FF (0.677), when compared with the value of MAPbI₃ device (0.644). These photovoltaic parameters directly resulted in a stunning PCE of 15.5% in α -FAPbI₃ device, higher than the PCE of 13.5% in prototypical MAPbI₃ cell.

3.2. High-quality α -FAPbI $_3$ layers for outstanding photovoltaic performance

3.2.1. DMSO-mediated intramolecular exchange for uniform α -FAPbI₃ Solvent engineering that involves formation of MAI-PbI₂-DMSO intermediate phase has led to dense and uniform perovskite layers, as previously realized by Jeon et al. [20]. Nonetheless, such method regretfully results in uncontrollably rough FAPbI₃ surface with pinholes [66], and thus incomparable photovoltaic performance with MAPbI₃ based devices so far [66,103-107]. Nonetheless, Yang and coworkers demonstrated that instead of forming FAI-PbI₂-DMSO intermediate prior to the crystallization of FAPbI₃ with thermal treatment, PbI₂(DMSO) precursor was first deposited on FTO/glass substrates, which then underwent reaction with FAI to generate high-quality, phase-pure FAPbI₃ films with excellent photovoltaic performance via intramolecular exchange between DMSO molecules and FAI compound (Fig. 8a) [66]. The DMSO intercalated PbI2 phases were initially confirmed by XRD patterns as shown in Fig. 8(b), where PbI₂(DMSO)₂ (upper pattern) was first obtained by precipitation from DMSO solution with toluene as the antisolvent; an equivalent of DMSO was then removed under

vacuum annealing at 60 °C, which produced desired PbI₂(DMSO) powder crystalline (middle pattern). Crucially, PbI₂(DMSO) could be retrieved after dissolution and spin-coating from solution with DMF as the solvent, thereby resulting in workable thin film with matched phase (lower pattern) with powder format (middle pattern) [66]. Next, FAI/isopropanol solution was spin-coated upon the PbI₂(DMSO) layer to form perovskite FAPbI₃, whose phase was unambiguously proven by XRD patterns shown in Fig. 8(c) and agreed well with previous reports [67,72]. In contrast to conventional PbI₂ + FAI two-step method that required high-temperature annealing to achieve perovskite α -FAPbI₃, DMSO-intercalated PbI₂ rapidly reacted with FAI through molecular exchange and generated pure α -FAPbI₃ films and exhibited better photovoltaic properties [66]. As shown in Fig. 8(d), unreacted PbI2 and FAI (denoted as "#" and "*", respectively) could still be found after the conventional two-step fabrication process (blue), while method based on PbI₂(DMSO) complex clearly resulted in exclusive perovskite phase α -FAPbI₃ (red). As shown in Fig. 8(e), while conventional fabrication achieved \sim 22 mA cm⁻² and \sim 1.03 V as J_{sc} and V_{oc} , respectively, DMSO-mediated method resulted in \sim 24 mA cm⁻² and \sim 1.05 V of $J_{\rm sc}$ and $V_{\rm oc}$, as well as a higher fill factor, which effectively contributed to an average PCE of ~19.5%, with top PCE exceeding 20% for solar cells fabricated based on PbI2(DMSO) complex, in contrast to ~14.5% average PCE for devices processed with conventional $PbI_2 + FAI$ method [66].

What accounts for the superior photovoltaic performance of perovskite FAPbI₃ devices based on PbI₂(DMSO) complex are the compact, flat and uniform FAPbI₃ films with densely covered large grains, where defect densities and boundary effects were



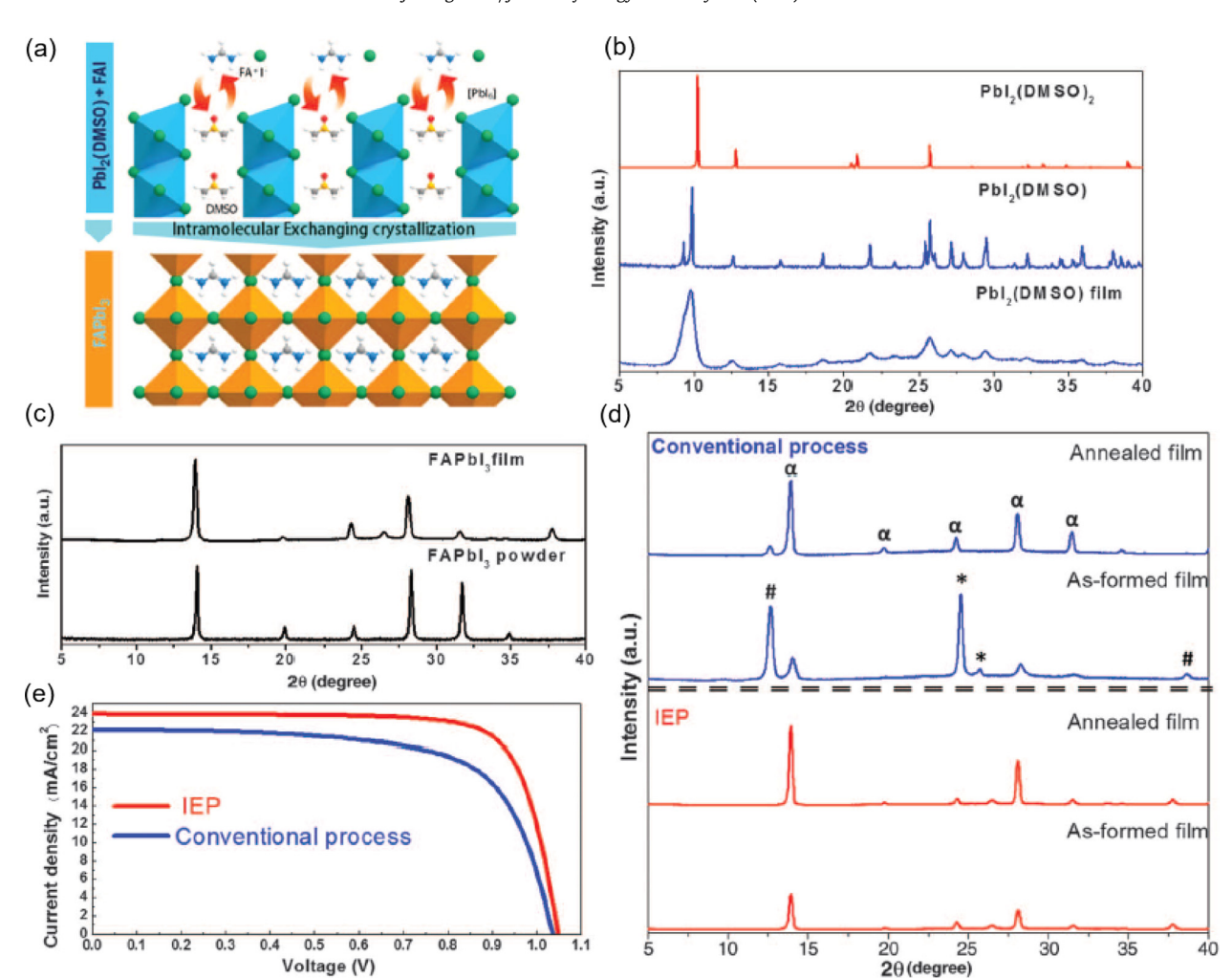


Fig. 8. Intramolecular exchange, precursors, structures, photovoltaic properties of α -FAPbl₃ [66]. (a) Schematic illustration of intramolecular exchange between interlayer DMSO molecules in Pbl₂(DMSO) and FAI to form α -FAPbl₃. (b) XRD patterns of Pbl₂(DMSO)₂ powder crystalline (top), Pbl₂(DMSO) powder crystalline (middle) and deposited Pbl₂(DMSO) film (bottom), showing different crystal structures between Pbl₂(DMSO)₂ and Pbl₂(DMSO), but same between powder crystalline and film formats of Pbl₂(DMSO). (c) XRD patterns of as-synthesized α -FAPbl₃ thin film fabricated from intramolecular exchange method (top), in comparison with α -FAPbl₃ powder (bottom). Strong diffraction peaks at around 13.9° and 28.1° respectively indicate preferential crystallographic orientations toward (10–1) and (202) directions in α -FAPbl₃ thin film [60]. (d) Comparison of XRD patterns of α -FAPbl₃ thin films fabricated from conventional Pbl₂+FAI two-step process (blue) and intramolecular exchange method (red), where α , and # denote structures of perovskite FAPbl₃, FAI and Pbl₂, respectively. (e) J-V curves of FAPbl₃ PSCs fabricated with conventional Pbl₂+FAI process (blue) and intramolecular exchange method (red). © AAAS. Reprint with permission granted by AAAS from ref. [66]. Permission to reuse must be obtained from the copyright holder.

minimized, and therefore favored efficient charge separation and long-distance carrier diffusion [108]. As shown in Fig. 9(a), the cross-section SEM image of a photovoltaic device indicates thick (>500 nm) and compact perovskite FAPbI₃ layer, which benefited phenomenal light absorption up to 840 nm [66,103]. Also, the average grain size of PbI₂(DMSO)-based FAPbI₃ film can easily surpass 500 nm (Fig. 9b upper part), different from the smaller grain size that falls below 500 nm as obtained from conventional PbI₂ + FAI fabrication process (Fig. 9b lower part). Furthermore, as shown in Fig. 9(c) left part, negligible hysteresis occurred on PbI₂(DMSO)based FAPbI₃ device, as revealed by forward (blue) and reverse (red) J-V scans, which can be ascribed to the largely annihilated trap state density in high-crystallinity FAPbI₃ film [108], as well as charge-delocalized FA+ that formed balanced electrostatic attraction with inorganic PbI₃⁻ framework [66]. The optoelectronic profile of perovskite FAPbI3 device was additionally validated by incident photon-to-current efficiency (IPCE), measured in external quantum efficiency (EQE) (black) as shown in Fig. 9(c) right part, where EQE is greater than ~85% in the range from 400 nm to 780 nm; after 840 nm, EQE falls to 0, corresponding to a 1.47 eV optical bandgap [66,103]. By integrating from 300 nm to 900 nm

of photons, integrated J_{sc} (red) showed a \sim 24 mA cm⁻², agreeing well with the value extracted from J–V curves shown in Fig. 9(c) left part [66].

3.2.2. $HPbI_3$ precursor for uniform $\alpha\text{-FAPbI}_3$ thin film with high surface coverage

Similar to the motif of Pbl₂(DMSO), Wang et al. [109] showed that HI can be used to intercalate Pbl₂ layered structure to form reactive HPbl₃, as shown in Fig. 10(a); and it subsequently enabled complete transition to FAPbl₃ by reacting with FAI. However, different from the 2-D \rightarrow 3-D conversion of Pbl₂(DMSO) \rightarrow α -FAPbl₃ without thermal treatment as realized in Yang's work [66], the transformation from precursor HPbl₃ to α -FAPbl₃ was in 3-D \rightarrow 3-D fashion and required thermal annealing [109], where the inorganic Pbl₃ $^-$ lattice framework was not tampered, and instead, only the organic cation exchange between H⁺ and FA⁺ occurred. After spin-coating the 1:1 molar ratio of HPbl₃/FAI solution in DMF, followed by annealing at 130 °C for 30 min and 160 °C for 60 min, black α -FAPbl₃ was formed [109], whose structure was characterized by XRD pattern as shown in Fig. 10(b), where strong diffraction peaks were observed at around $2\theta = 14^\circ$, 28° , indicating preferred

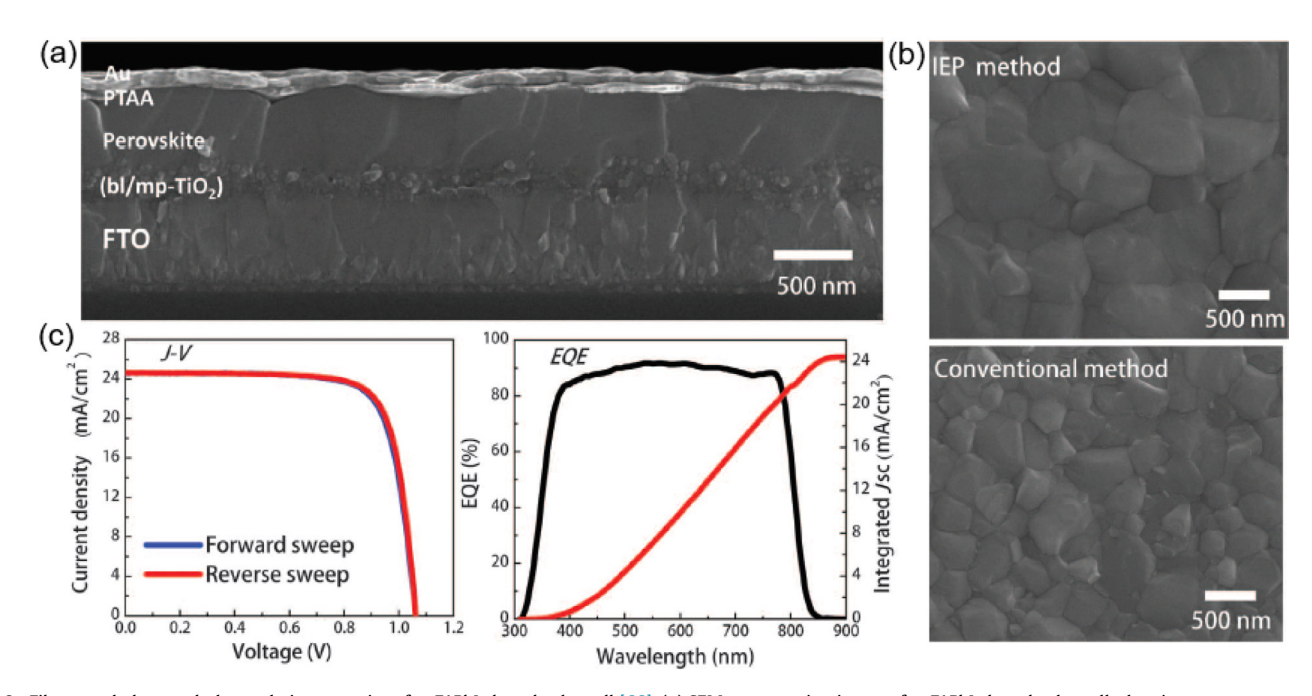


Fig. 9. Film morphology and photovoltaic properties of α -FAPbl₃ based solar cell [66]. (a) SEM cross-section image of α -FAPbl₃ based solar cell, showing a compact perovskite layer with thickness greater than 500 nm. (b) Surface morphology of FAPbl₃ layer fabricated by intramolecular exchange process (top), by conventional Pbl₂+FAI method (bottom). By comparison, intramolecular exchange process led to dense FAPbl₃ layer with large grains, while grain size from conventional process was smaller. (c) J–V curves of α -FAPbl₃ device fabricated from intramolecular exchange process with forward (blue) and reverse (red) voltage scans (left), IPCE spectrum (black) along with integrated J_{sc} (red) (right). The overlapped J–V curves indicated hysteresis-free behavior of solar cell. © AAAS. Reprint with permission granted by AAAS from ref. [66]. Permission to reuse must be obtained from the copyright holder.

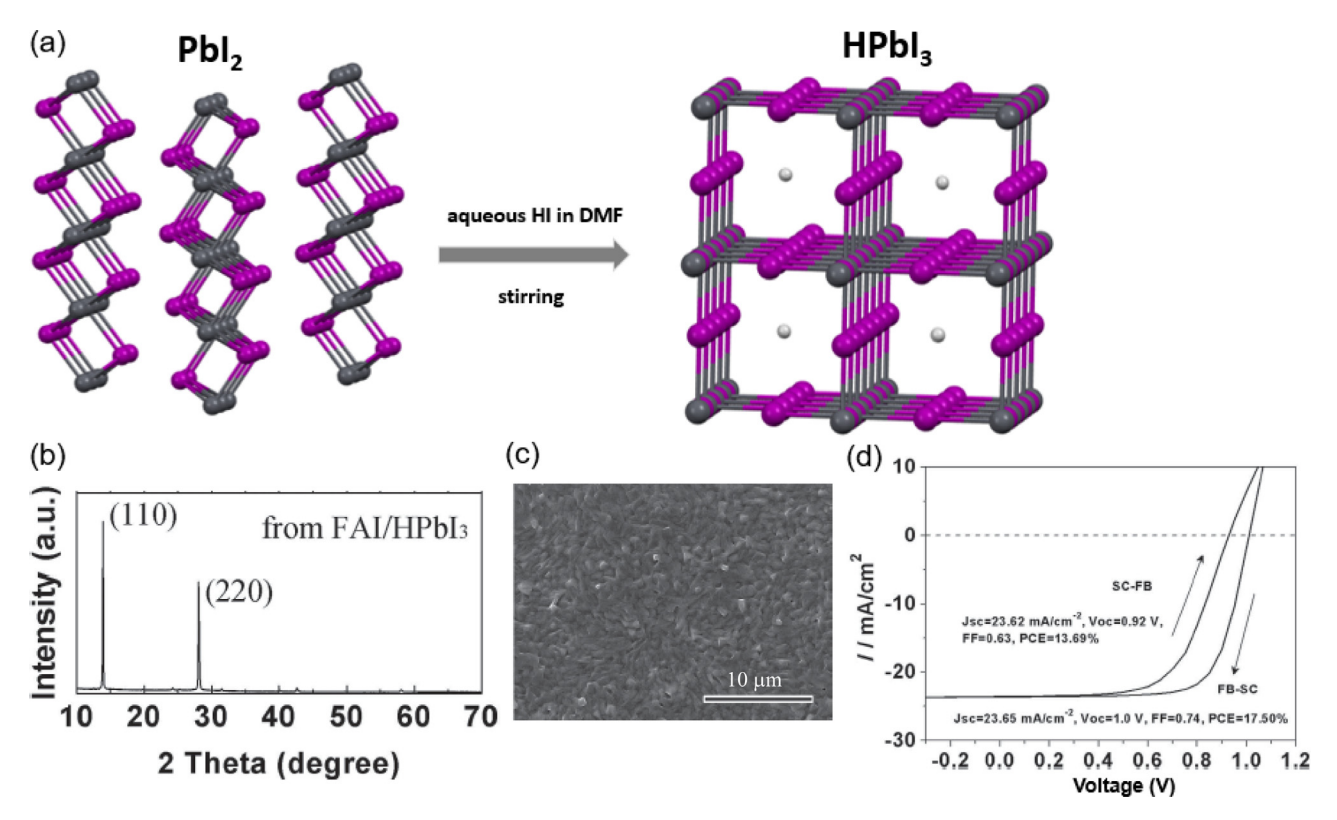


Fig. 10. Depictive scheme, structural, morphological and photovoltaic characterizations of FAI/HPbl₃ converted FAPbl₃. (a) Schematic depiction of HPbl₃ formation from reacting Pbl₂ with HI in DMF. (b) XRD pattern of perovskite FAPbl₃ thin film deposited from FAI/HPbl₃ precursor solution [109]. (c) SEM surface image of α-FAPbl₃ prepared from FAI/HPbl₃ precursors [109]. (d) J–V curves of α-FAPbl₃ PSC based on forward (SC-FB) and reverse (FB-SC) voltage scans, with extracted solar cell performance parameters included [109]. © John Wiley and Sons. Reprint with permission granted by John Wiley and Sons from ref. [109]. Permission to reuse must be obtained from the copyright holder.

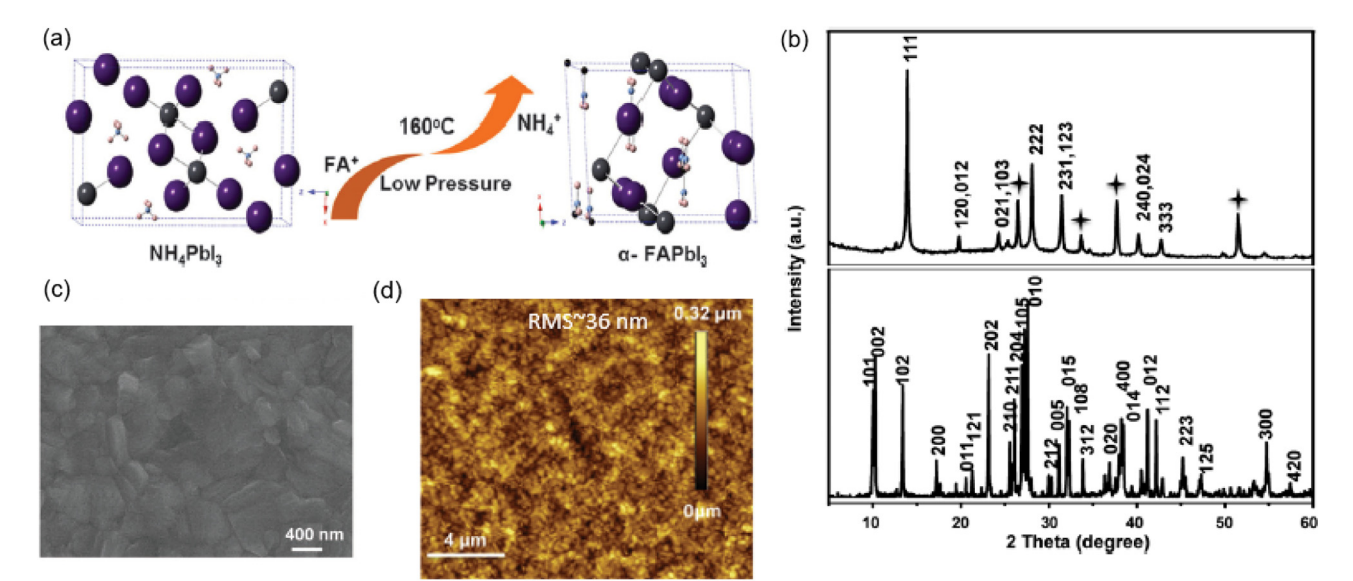


Fig. 11. Reaction scheme, structural and morphological characterizations of α -FAPbl₃ [75]. (a) Schematic illustration of transformation from NH₄Pbl₃ to α -FAPbl₃ via cation exchange under 160 °C and low pressure condition. (b) XRD patterns of NH₄Pbl₃ thin film (top) and α -FAPbl₃ thin film (bottom). (c,d) SEM and AFM images of α -FAPbl₃ film surface, showing densely covered large grains and a root mean square roughness of ~36 nm. © Royal Society of Chemistry (RSC). Reprint with permission granted by RSC from ref. [75]. Permission to reuse must be obtained from the copyright holder.

crystallographic orientations toward (110), (220) directions, respectively [109,110]. As shown in Fig. 10(c), α -FAPbI₃ film deposited from HPbI₃/FAI solution had a dense and uniform surface, and it led to superior solar cell performance with PCE of 13.69% in forward J–V scan, characteristic of $J_{\rm SC}$ as 23.62 mA cm⁻², $V_{\rm OC}$ as 0.92 V and FF as 0.63; while a PCE of 17.50%, featured with $J_{\rm SC}$ as 23.65 mA cm⁻², $V_{\rm OC}$ as 1.0 V and FF as 0.74, was achieved from reverse J–V scan, as indicated in Fig. 10(d).

10

3.2.3. $NH_4{}^+/FA^+$ cation exchange for flat $\alpha\text{-FAPbI}_3$ thin film with densely packed large grains

Apart from H+ that exchanged with FA+ to generate highquality FAPbI3 films with high surface coverage, as realized in previous work [109], Zhou et al. [75] demonstrated that NH₄PbI₃ can undergo substitution reaction with formamidine acetate (FAac) to form pure and uniform α -FAPbI $_3$ at HT condition, as shown in Fig. 11(a). To illustrate the change in crystal structure, XRD was performed on thin-film NH₄PbI₃, and α-FAPbI₃ after cation exchange reaction. As shown in Fig. 11(b), XRD pattern of NH₄PbI₃ (upper) displays different peaks when compared with the synthesized α -FAPbI₃ (lower) [75,107,111], thus indicating altered material structure after cation exchange. Noteworthily, the peaks marked with cross signs indicate TiO2 substrate signals. Surface morphology of fabricated α -FAPbI₃ thin film was then characterized by SEM and Atomic Force Microscopy (AFM). As shown in Fig. 11(c), SEM image displays a uniform surface of α -FAPbI₃ thin film with densely filled large grains (~400 nm); and AFM topographical image, as shown in Fig. 11(d), shows a relatively flat surface profile with a root mean square roughness as 36 nm.

J–V measurements were then conducted to examine the photovoltaic properties of fabricated α -FAPbI $_3$ based solar cell. As shown in Fig. 12(a), α -FAPbI $_3$ device exhibited nearly hysteresis-free photovoltaic performance, where forward and reverse J–V sweeps all resulted in the same PCE as 12.4%. Phenomenally, a $J_{\rm SC}$ of 22.2 mA cm $^{-2}$, $V_{\rm oc}$ of 0.94 V and FF of 0.59 were derived from the reverse scan; closely, a $J_{\rm SC}$ of 22.3 mA cm $^{-2}$, $V_{\rm oc}$ of 0.95 V and FF of 0.58 were extracted from the forward scan. The greatly reduced hysteresis on FAPbI $_3$ device, as fabricated from the NH $_4$ +-FA+ exchange method, can be partially attributed to the annihilated trap state densities in α -FAPbI $_3$ [47,108], as due to the large and dense grains

that outweigh the grain boundary effects, as well as the charge-delocalized FA+ that mitigated the ferroelectric polarization in the FAPbI $_3$ system [35,112]. Remarkably, α -FAPbI $_3$ also exhibited significantly greater thermal stability. As shown in Fig. 12(b) (black curve), FAPbI $_3$ film annealed at 140 °C for up to 7 h showed no obvious degradation in PCE of fabricated solar cell, where the inset SEM image (upper right) displayed a similar morphology to the asfabricated film surface as shown in Fig. 11(c); nonetheless, in terms of MAPbI $_3$ film (red curve), degradation in PCE of solar cell started to appear at 2 h of annealing at 140 °C, and drastic decrease of PCE started from 4 h of thermal treatment. By 7 h of thermal annealing, MAPbI $_3$ based solar cell retained only 5% of original performance, with the inset SEM image (lower left) showing a cracked surface of MAPbI $_3$ thin film.

3.2.4. HI-additive induced uniform α -FAPbI $_3$ thin film with high surface coverage

It is well known that PbI2 has limited solubility in DMF and γ -butyrolactone (GBL), which has been attributed as a main reason for poor photovoltaic performance of fabricated PSCs [113-116]. Nevertheless, it was previously shown that chemical additive-modified soluble PbI2, and the adoption of aqueous soluble Pb²⁺ source effectively facilitated formation of uniform and dense perovskite layers with high surface coverage, and consequently led to formidable photovoltaic performance of fabricated solar cells. These were realized in tetra-n-butylammonium triiodide (TBAI₃)-additive doped PbI₂ layer fabrication followed by subsequent reaction with MAI to form smooth and dense MAPbI₃ films [114], and aqueous Pb(NO₃)₂-precursor based MAPbI₃ systems [115]. In fact, the practices of adopting PbI₂(DMSO), HPbI₃ precursors essentially promote the dissolution of lead (II) precursor, and therefore led to complete conversion of lead (II) precursor to perovskites, as detailed in abovementioned sections [66,109]. Being a strong acid that provides abundant concentration of iodide ions, HI has potential to promote dissolution of PbI2 and generates high-quality FAPbI₃ thin films [101]. Eperon and coworkers successfully demonstrated that HI-added perovskite precursor solution could generate uniform and dense FAPbI3 film as shown in Fig. 13(a), in contrast to FAPbI₃ film without HI in precursor solution that had low surface coverage, as shown in Fig. 13(b) [71]. With HI

Please cite this article as: J. Gong et al., Cation engineering on lead iodide perovskites for stable and high-performance photovoltaic applications, Journal of Energy Chemistry (2018), https://doi.org/10.1016/j.jechem.2017.12.005

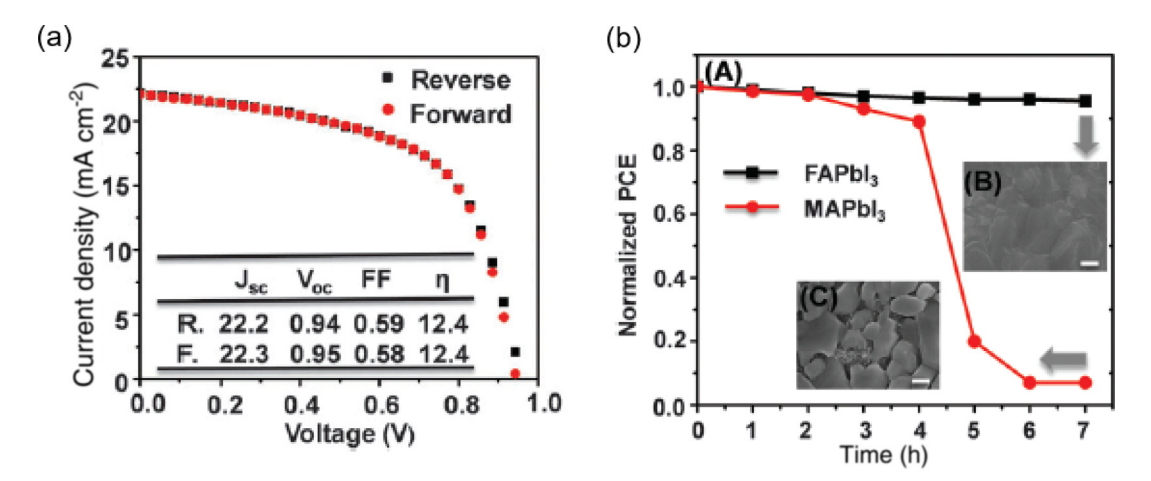


Fig. 12. Photovoltaic properties and thermal stabilities of α -FAPbl₃, MAPbl₃ thin films [75]. (a) J–V curves of α -FAPbl₃ based solar cell as fabricated from NH₄+-FA+ exchange method, with forward and reverse scans shown in red and black dots, respectively, while inset displays extracted photovoltaic parameters. Conformed curves indicate the absence of hysteresis. (b) PCEs of solar cells based on α -FAPbl₃ (black), MAPbl₃ (red) thin films thermally annealed at 140 °C for different lengths of time, with inset photographs showing films surface of α -FAPbl₃ (B), MAPbl₃ (C) after annealing at 140 °C for 7 h. © RSC. Reprint with permission granted by RSC from ref. [75]. Permission to reuse must be obtained from the copyright holder.

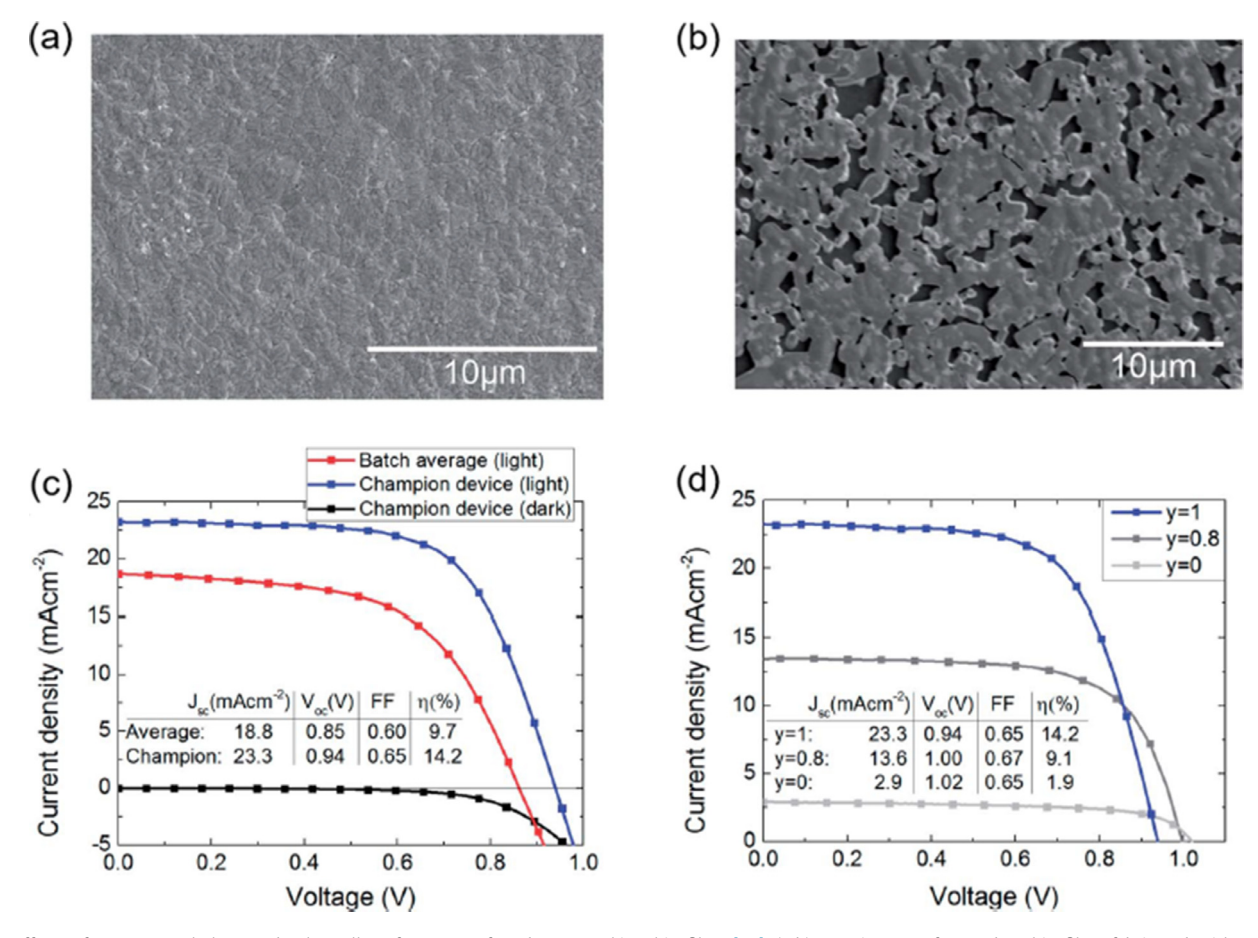


Fig. 13. Effects of HI on morphology and solar cell performance of FAPbI₃ perovskite thin films [71]. (a,b) SEM images of α -FAPbI₃ thin films fabricated with, without HI added in FAI/PbI₂ precursor solutions, respectively. (c) J–V curves of perovskite FAPbI₃ based solar cells with best performing device (blue), batch average device (red) and dark characteristics (black); inset displays derived photovoltaic parameters. (d) J–V curves of FAPb(I_yBr_{1-y})₃ based devices with halide contents y=1, y=0.8, y=0 shown in blue, dark gray, light gray, respectively. As iodide content decreases, monotonic decrease in J_{sc} and PCE, but increase in V_{oc} can be seen in inset J–V parameters. © RSC. Reprint with permission granted by RSC from ref. [71]. Permission to reuse must be obtained from the copyright holder.

12

in precursor solution, resultant FAPbI3 based solar cell exhibited phenomenal photovoltaic properties. As shown in Fig. 13(c), J-V curves of α -FAPbI₃ devices impart a top PCE as 14.2% with 23.3 mA cm⁻², 0.94V and 0.65 as J_{sc} , V_{oc} and FF, respectively; an average PCE of 9.7% was derived, with $18.8 \,\mathrm{mA} \,\mathrm{cm}^{-2}$, $0.85 \,\mathrm{V}$ and $0.60 \,\mathrm{as}$ J_{sc} , V_{oc} and FF, respectively. For mixed-halide FAPb($I_{\nu}Br_{1-\nu}$)₃, as shown in Fig. 13(d), 100% iodide content perovskite (y = 1, blue) represented the reference champion FAPbI₃ cell that showed 14.2% PCE; when y = 0.8 (gray), FAPbI_{2.4}Br_{0.6} exhibited decreased PCE as 9.1% with J_{sc} , V_{oc} and FF being 13.6 mA cm⁻², 1.00 V and 0.67, respectively; After y continued to decrease to 0, corresponding FAPbBr₃ device showed significantly degraded photovoltaic performance with only 1.9% of PCE, and $2.9\,\mathrm{mA}~\mathrm{cm}^{-2}$, $1.02\,\mathrm{V}$ and $0.65\,\mathrm{m}$ of J_{sc} , V_{oc} and FF, respectively. The monotonic decrease in PCE and $J_{\rm sc}$, but increase in $V_{\rm oc}$, illustrated the widened optical bandgaps in $FAPb(I_yBr_{1-y})_3$ perovskites with greater Br contents, agreeing well with previous observations [9,22,58,59,117–119].

4. Mixed-cation perovskites for stable and formidable photovoltaic performance

4.1. Perovskites (MA+,Cs+)PbI₃

4.1.1. MA+, Cs+ alloyed lead iodide for thermally stable perovskite materials

Due to the high decomposition temperatures of Cs⁺-based inorganic perovskites, such as CsPbI₃ and CsPbBr₃ [120-123], Cs⁺ has the potential to enhance the thermal stabilities of alloyed hybrid perovskites. As such, we synthesized MAPbI₃ and MA_{0.95}Cs_{0.05}PbI₃ thin films, which were thermally treated at various temperatures with 10 min of equilibration time at each set temperature. Optical reflectance spectra were then measured on these two films after treatment of each set temperature, and their thermal stabilities were evidenced from the evolutions of temperature-dependent reflectance spectra. As shown in Fig. 14(a), regular MAPbI₃ thin film experienced phenomenal degradation after being thermally treated at 190 °C for 10 min, as indicated by the upshift of reflectance from 500 nm to 750 nm and considerably decreased slope of onset portion between 750 nm and 800 nm, when compared with the reflectance profiles measured after treatments at lower temperatures; while at 200 °C treatment for 10 min, MAPbI₃ thin film exhibited further degradation, as illustrated by the largely elevated reflectance from 500 nm to 750 nm along with an apparently diminished onset area, and thus signifying a massive loss of light-harvesting activity of perovskite. Nevertheless, as displayed in Fig. 14(b), no obvious change in reflectance spectra was observed on MA_{0.95}Cs_{0.05}PbI₃ thin film after thermally treated at set temperatures up to 200 °C, where the slope of reflectance onset between 750 nm and 800 nm was largely unaffected. To quantify the change in optical absorption ability of thermally treated thin films, optical bandgaps were extrapolated from Tauc plots of corresponding reflectance spectra. As shown in Fig. 14(c), after 200 °C treatment for 10 min (red), degraded film had a 2.35 eV bandgap, in contrast to original 1.54 eV bandgap on as-developed MAPbI₃ thin film (black); whereas for MA_{0.95}Cs_{0.05}PbI₃ thin film, as shown in Fig. 14(d), 1.52 eV bandgap was observed after 200 °C treatment (red), which was only 0.01 eV widened relative to 1.51 eV on as-developed thin film (black). The retained reflectance profiles of MA_{0.95}Cs_{0.05}PbI₃ thin film illustrated its significantly enhanced thermal stability, in comparison with pristine MAPbI₃.

4.1.2. MA+, Cs+ alloyed lead iodide for stable and improved photovoltaic properties

By performing time-resolved photoluminescence (TRPL), we demonstrated that incorporation of Cs⁺ can lead to prolonged bulk carrier lifetimes in MA_{0.95}Cs_{0.05}PbI₃ crystals, in comparison

with pristine MAPbI₃ crystals, with crystals grown from corresponding solutions with stoichiometric MAI, CsI and PbI₂ precursors by following method reported in work [124]. As shown in Fig. 15(a), three MAPbI₃ crystals as grown in the same batch exhibited longer fast-component carrier lifetimes (τ_1 , crystal #1: 7.2 ns, crystal #2: 8.3 ns, crystal #3: 9.6 ns) than the $MA_{0.95}Cs_{0.05}PbI_3$ crystals (crystal #1: 3.0 ns, crystal #2: 2.3 ns, crystal #3: 2.2 ns), but shorter slow-component carrier lifetimes (τ_2 , crystal #1: 56.1 ns, crystal #2: 44.8 ns, crystal #3: 93.3 ns; with MA_{0.95}Cs_{0.05}PbI₃ having 129.4 ns, 160.1 ns and 143.0 ns for crystals #1, #2 and #3, respectively). This indicated a slightly increased trap-assisted carrier recombination, but largely delayed free carrier recombination process [125,126], which was expected to have positive effects on solar cell performance based on Cs+, MA+ alloyed perovskites. Indeed, Niu and coworkers previously demonstrated that mixed-cation (MA,Cs)PbI₃ based device exhibited improved photovoltaic performance [127]. As shown in Fig. 15(b), MA_{0.91}Cs_{0.09}PbI₃ based champion solar cell (red) had a J_{sc} of 22.57 mA cm⁻², V_{oc} of 1.06 V and FF of 0.76, which were correspondingly greater than the $J_{\rm sc}$ of 20.59 mA cm⁻², $V_{\rm oc}$ of 1.04 V and FF of 0.74 as achieved on pristine MAPbI3 champion cell (black). The difference in photovoltaic parameters eventually led to a 18.1% PCE in champion $\rm MA_{0.91}Cs_{0.09}PbI_3$ cell, and only 15.8% on champion $\rm MAPbI_3$ cell. Also, the thermal stabilities of MA_{0.91}Cs_{0.09}PbI₃ and MAPbI₃ cells were studied from respective photovoltaic performance as aged in thermal conditions [127]. As shown in Fig. 15(c), unencapsulated MAPbI₃ device (black) underwent continuous decrease in PCE as aged at 85 °C in air; and by 60 min of aging, device exhibited only ~30% of original performance. While for unencapsulated MA_{0.91}Cs_{0.09}PbI₃ device (red) that was aged under the same condition, no obvious deterioration of cell performance was witnessed by 40 min of aging at 85 °C; and after 60 min of aging, ~85% of original performance could still be retained. The optoelectronic structures of MAPbI₃ and MA_{0.91}Cs_{0.09}PbI₃ champion devices were then examined by IPCE spectra, as shown in Fig. 15(d), where IPCE% of $MA_{0.91}Cs_{0.09}PbI_3$ was greater than $MAPbI_3$ between 400 nm and 750 nm and therefore signified a greater quantum conversion efficiency in the visible spectrum. Due to the IPCE spectra of both devices that showed a common onset area from 750 nm to 800 nm and 0% quantum efficiency after ~810 nm, it can be imparted that MA_{0.91}Cs_{0.09}PbI₃ and MAPbI₃ perovskites had similar optical bandgaps. Noteworthily, by integrating from 350 nm to 850 nm, the integrated J_{sc} of $MA_{0.91}Cs_{0.09}PbI_3$ device was at ~20 mA cm⁻², correspondingly greater than MAPbI₃ device at \sim 18.7 mA cm⁻², closely matching the values derived from Fig. 15(b).

4.2. MA+, FA+ mixed-cation systems for stable and improved solar cell performance

With smaller ionic radius than FA+ (279 pm) [75,100], MA+ (270 pm) can decrease the tolerance factors of MA+/FA+ mixedcation lead iodide structures, and thereby forming phase-stable perovskite materials, as previously demonstrated by Dai and coworkers [128]. Fig. 16(a) shows photographs of solution-grown FA_{1-x}MA_xPbI₃ thin films, with samples from left to right respectively corresponding to compositions of x = 0, 0.2, 0.4, 0.6, 0.8 and 1.0. Clearly, with the presence of MA+ in precursor solutions, synthesized FA_{1-x}MA_xPbI₃ thin films were in black colors, and therefore indicated the photoactive perovskite phases. However, when there was no MA⁺ in reaction solution (100 mol% FAI precursor), non-perovskite phase δ -FAPbI $_3$ was directly resulted, as demonstrated by the yellow color of sample. The crystal structures were further confirmed by XRD patterns, as shown in Fig. 16(b). With 100 mol% FAI precursor, as-formed FAPbI₃ had a hexagonal structure, whose diffraction pattern (dark yellow) agrees well with pre-

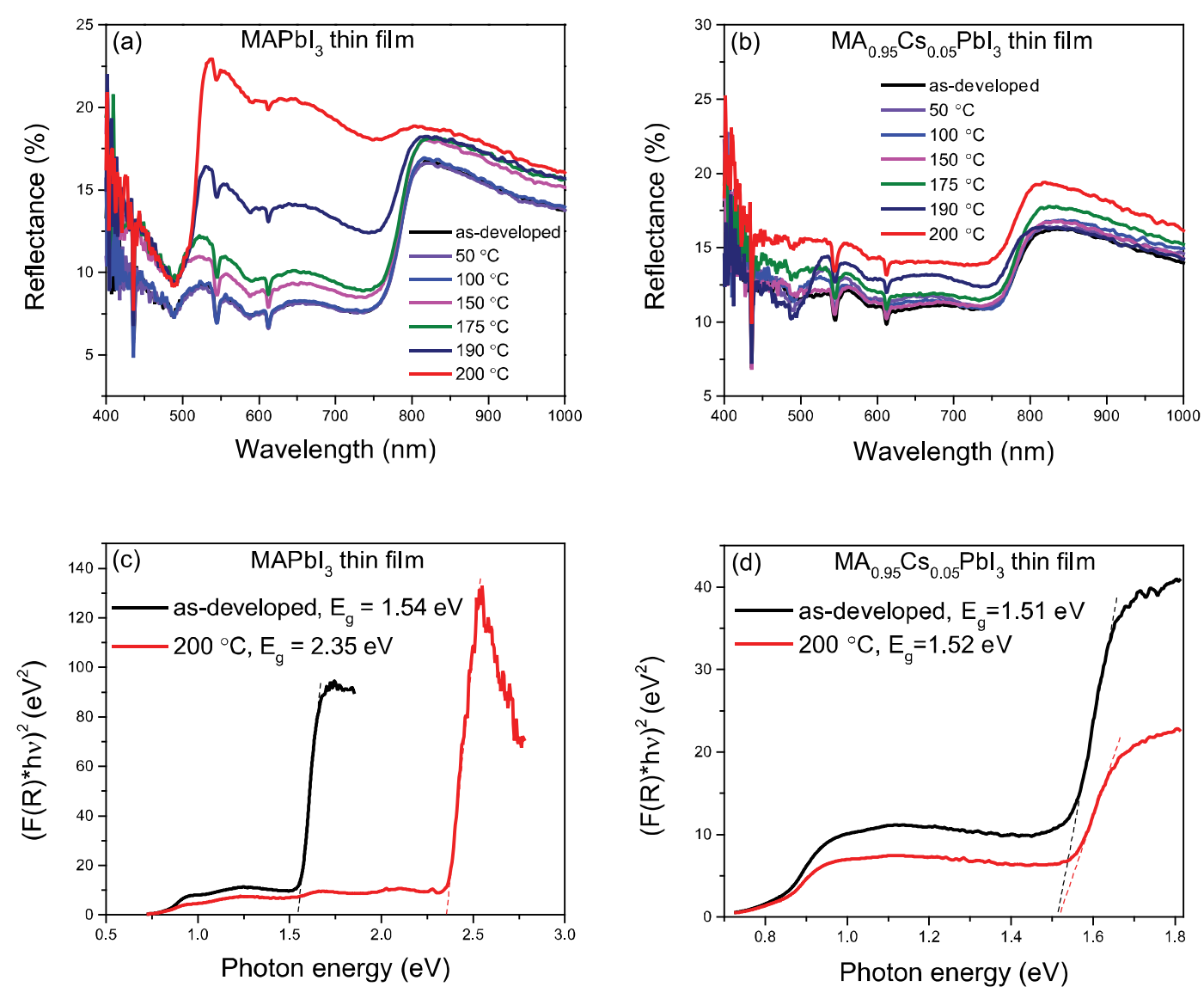


Fig. 14. Temperature-dependent optical reflectance spectra of MAPbl₃ and $MA_{0.95}Cs_{0.05}Pbl_3$ thin films and corresponding Tauc plots. (a,b) Evolution of optical reflectance spectra of MAPbl₃, $MA_{0.95}Cs_{0.05}Pbl_3$ thin films, respectively, as set temperature rose from as-developed temperature (RT) to 200 °C. (c,d) Corresponding Tauc plots of the reflectance spectra shown in (a,b), respectively, with only RT and 200 °C shown for clear comparison of extrapolated optical bandgaps.

viously reported studies [60,72,100,101]. At 20 mol.% MAI and 80 mol% FAI stoichiometric cation precursors, as-grown material occupied a mixed hexagonal/cubic structure, which was illustrated through the co-existence of diffraction peaks at around 11.2°, 26.2° that are characteristic of hexagonal phase, and at around 14°, 20°, 24.5°, 28°, 31.7° that are characteristic of perovskite structures (magenta pattern) [60,72,100,101]; while at 40 mol%, 60 mol% and 80 mol% MAI, pure cubic phases of alloyed perovskites were unambiguously obtained (dark cyan, blue and red patterns). In addition, when cation iodide precursor was 100 mol% MAI, tetragonal MAPbI₃ was crystallized, which was manifested in the (002)/(110) doublet peak at around 14° as well as (004)/(220) structure at around 28° (black pattern) [60]. Furthermore, due to the fact that FA+ has larger size than MA+, incorporation of FA+ led to enlargements of material lattice constants, which was illustrated in the (100)/(110) peaks that shifted toward smaller 2θ angles due to $d = n\lambda/2\sin\theta$ as FA⁺ content increased in alloyed systems (Fig. 16c and d).

Apart from the stabilization effects of $FA_{1-x}MA_xPbI_3$ perovskite structures, MA^+/FA^+ co-cationed lead iodide perovskites also exhibited synergistically improved optoelectronic properties. As pre-

viously proved by Zhang et al. [129], incorporation of FA+ led to redshift in PL peak wavelengths, which was an indication of narrowed optical bandgaps (Fig. 16e). This is justified with the smaller bandgap associated with pristine $\alpha\text{-FAPbI}_3$ (<1.48 eV) when compared with MAPbI₃ (\sim 1.53 eV) [59,67,68]. Also, as shown in Fig. 16(f), such widened optical absorption was accompanied with prolonged carrier lifetimes, where pristine MAPbI₃, FA_{0.1}MA_{0.9}PbI₃, FA_{0.2}MA_{0.8}PbI₃ and FA_{0.3}MA_{0.7}PbI₃ exhibited carrier lifetimes of 11 ns, 14 ns, 17 ns and 16 ns, respectively. In terms of the solar cell performance, FA_{0.1}MA_{0.9}PbI₃ based device exhibited significantly enhanced photovoltaic properties when compared to pure MAPbI₃ counterpart. As shown in Fig. 16(g), FA_{0.1}MA_{0.9}PbI₃ based device showed a 20.26% PCE, characteristic of a Jsc, Voc and FF as 23.61 mA cm⁻², 1.08 V and 0.796, respectively; in contrast, MAPbI₃ cell only had a 18.59% PCE with $23.45 \, \text{mA cm}^{-2}$, $1.05 \, \text{V}$ and 0.758as J_{sc}, V_{oc} and FF, respectively. In addition, FA_{0.2}MA_{0.8}PbI₃ based cell also demonstrated improved photovoltaic performance as compared to MAPbI₃ cell, where its PCE was achieved as 19.32% with corresponding J_{sc} , V_{oc} and FF as 22.54 mA cm⁻², 1.08 V and 0.794, respectively. Although it was slightly outperformed by MAPbI₃, FA_{0.3}MA_{0.7}PbI₃ device also showed a phenomenal photovoltaic

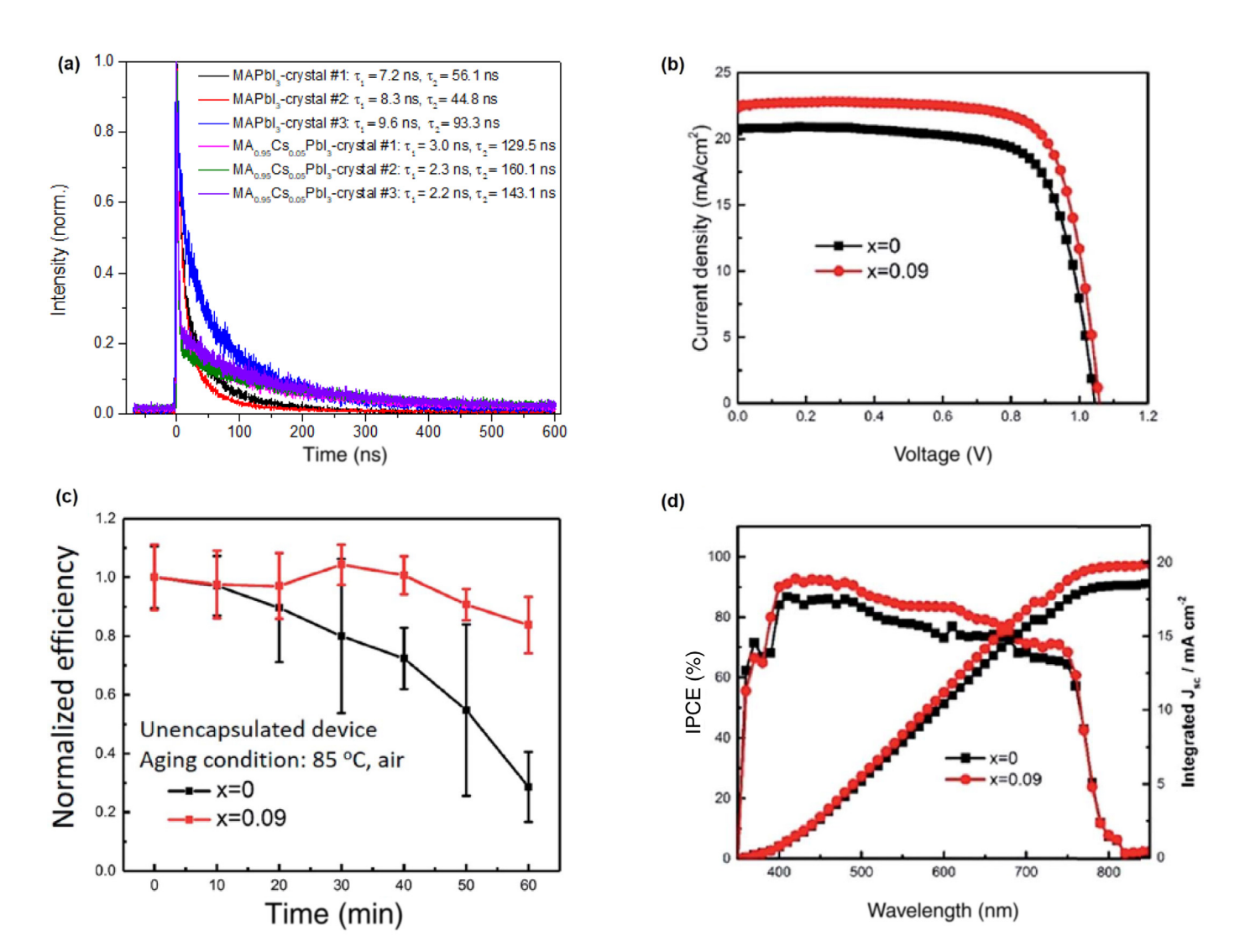


Fig. 15. Carrier recombination dynamics, photovoltaic properties, stability tests and IPCE spectra of MAPbl₃, (MA,Cs)Pbl₃ and fabricated solar cells. (a) Normalized TRPL decay spectra of MAPbl₃ crystals (black, red, blue) and MA_{0.95}Cs_{0.05}Pbl₃ crystals (magenta, green, violet). (b) J–V curves of MAPbl₃ (black), MA_{0.91}Cs_{0.09}Pbl₃ (red) based solar cells [127]. (c) Stability tests of unencapsulated MAPbl₃, MA_{0.91}Cs_{0.09}Pbl₃ based devices at 85 °C in air [127]. (d) IPCE spectra and integrated J_{sc} of MAPbl₃ (black), MA_{0.91}Cs_{0.09}Pbl₃ (red) based devices [127]. © RSC. Reprint with permission granted by RSC from ref. [127]. Permission to reuse must be obtained from the copyright holder.

performance, where a PCE, $J_{\rm SC}$, $V_{\rm OC}$ and FF of 17.29%, 22.50 mA cm⁻², 1.02 V and 0.752 were realized, respectively. The fact that FA_{0.1}MA_{0.9}PbI₃ had greater $J_{\rm SC}$ output or smaller optical bandgap than pristine MAPbI₃ formats was verified by the EQE spectra that are shown in Fig. 16(h), where larger photon-to-current quantum efficiency was observed from around 750 nm to 800 nm on FA_{0.1}MA_{0.9}PbI₃ based device (black) as compared to pure MAPbI₃ counterpart (red); while the integrated current density curves (dotted lines) further corroborated the $J_{\rm SC}$ extrapolated from Fig. 16(g), with obtained $J_{\rm SC}$ being 22.57 mA cm⁻² and 21.77 mA cm⁻² on FA_{0.1}MA_{0.9}PbI₃ and MAPbI₃, respectively.

4.3. FA^+ , Cs^+ alloyed lead iodide for stable and outstanding photovoltaic properties

As previously mentioned, due to Goldschmidt tolerance factors that deviate from 0.9–1 region, both perovskite $\alpha\textsc{-}\textsc{FAPbI}_3$ and $\alpha\textsc{-}\textsc{CsPbI}_3$ are not thermodynamically stable at RT [63,75,100,130]. However, Li and coworkers discovered that mixed-cation (FA,Cs)PbI_3 alloys were stabilized in photoactive $\alpha\textsc{-}\textsc{phase}$ through tuning the tolerance factor to between 0.8 and 1, and the

resulting perovskite alloy showed significantly improved stability and formidable solar cell performance when compared with pristine FAPbI₃ perovskite [63]. As shown in Fig. 17(a), as-fabricated FAPbI₃ film (red) showed both δ -FAPbI₃ and PbI₂, which are indicated by peaks at 11.5° and 12.5°, respectively; and after 30 days of storage in dry air (black), aged film displayed increased amounts of δ -FAPbI₃ and PbI₂, as evidenced by escalated peak intensities. Nevertheless, FA_{0.85}Cs_{0.15}PbI₃ thin film exhibited much improved phase stability by showing no δ -FAPbI₃ and PbI₂ just after fabrication (blue), and only trace amount of PbI₂ after 30 days of aging in dry air (green). To illustrate the change in light-harvesting ability of FA_{0.85}Cs_{0.15}PbI₃ alloyed perovskite over time, UV-vis absorbance was characterized on FA_{0.85}Cs_{0.15}PbI₃ thin film. As shown in Fig. 17(b), α -FA_{0.85}Cs_{0.15}PbI₃ experienced no noticeable change in absorption by the nearly conformed spectra as aged across 18 days, and hence demonstrated the greatly enhanced stability. J-V characterizations were then applied to study the photovoltaic properties of $FA_{0.85}Cs_{0.15}PbI_3$ alloy and pristine $FAPbI_3$ perovskites. As shown in Fig. 17(c), while pure FAPbI₃ based device experienced continuous deterioration of J_{sc} , V_{oc} as well as FF over 15 days' aging in dry air; FA_{0.85}Cs_{0.15}PbI₃ cell exhibited improvements of photo-

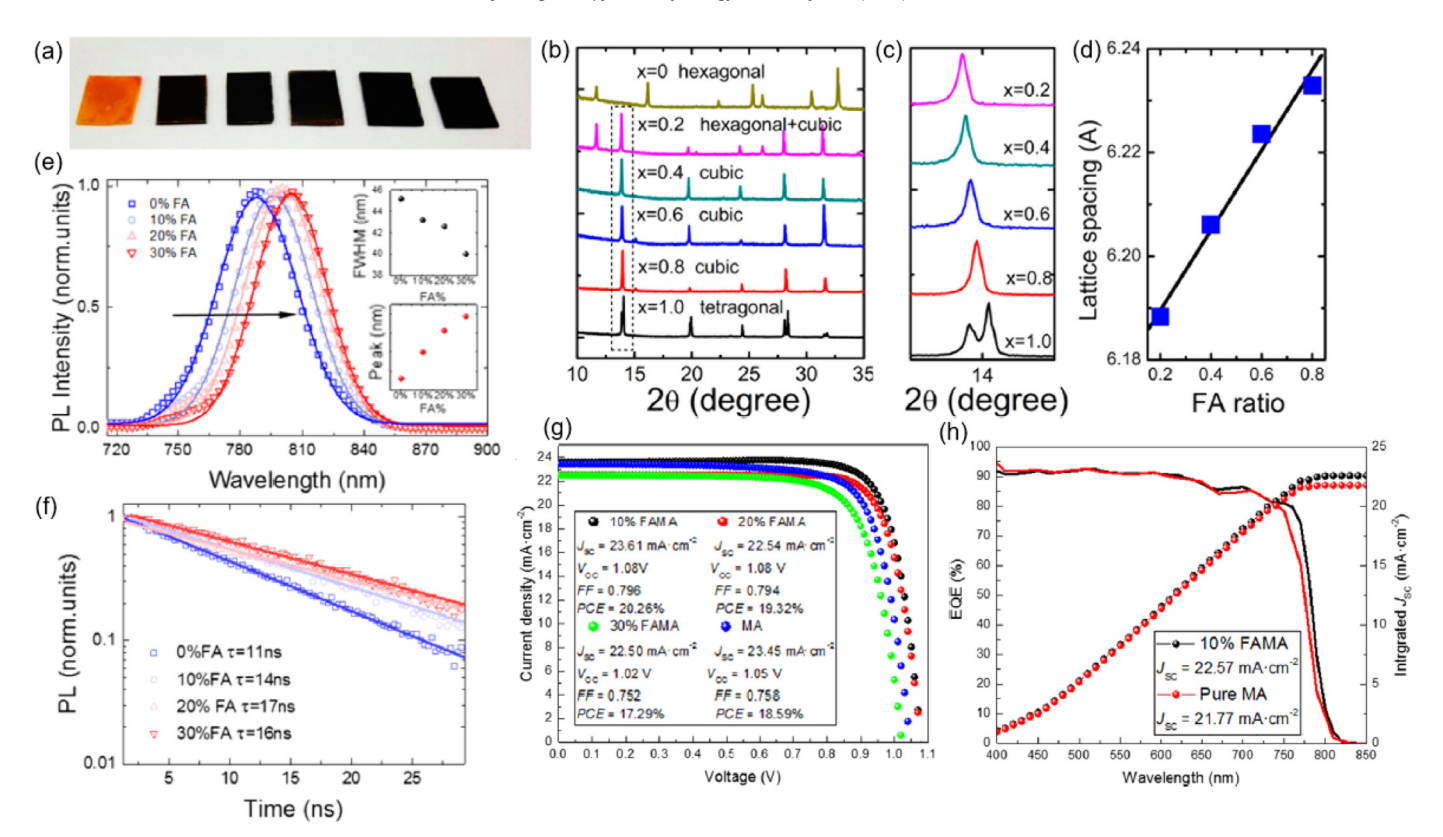


Fig. 16. Evolution of structural, optoelectronic and photovoltaic properties of $FA_{1-x}MA_xPbI_3$ perovskites. (a) Photographs of as-synthesized $FA_{1-x}MA_xPbI_3$ thin films, with x = 0, 0.2, 0.4, 0.6, 0.8, 1.0 corresponding to samples from left to right. (b, c) XRD patterns of $FA_{1-x}MA_xPbI_3$ thin films, evolution of (110) or (100) diffraction peaks (zoom-in view) with increasing x from top to bottom, respectively. (d) Calculated lattice spacing d with respect to FA composition (1-x). © ACS. Reproduced with permission granted by ACS from ref. [128]. (e) PL spectra of $FA_{1-x}MA_xPbI_3$ thin films with x = 1.0, 0.9, 0.8 and 0.7 corresponding to spectra from left to right; inset shows full width at half maximum and PL peak wavelength as a function of $FA_{1-x}MA_xPbI_3$ thin films with MA+ composition x = 1.0, 0.9, 0.8 and 0.7. (g) J-V curves of PSCs based on different cation compositions. (h) IPCE spectra and corresponding integrated J_{Sc} curves of devices based on $FA_{0.1}MA_{0.9}PbI_3$ (black) and MAPbI₃ (red) perovskites. © ACS. Reproduced with permission granted by ACS from ref. [129]. Permission to reuse must be obtained from the copyright holder.

voltaic performance during the first 3 days of aging, then experienced no noticeable change up to 15 days, as shown in Fig. 17(d). Also, $FA_{0.85}Cs_{0.15}PbI_3$ based cell showed J_{sc} and V_{oc} that are greater than 20 mA cm⁻² and 1.0 V, respectively, as tested within the same day of fabrication, while FAPbI₃ cell initially showed J_{sc} and V_{oc} that were slightly smaller than 20 mA cm⁻² and 1.0 V, respectively, along with a poorer FF. Eventually, the difference in the photovoltaic parameters between $FA_{0.85}Cs_{0.15}PbI_3$ and $FAPbI_3$ accounted for a top PCE of 17.3%, an average PCE of 16.1% on $FA_{0.85}Cs_{0.15}PbI_3$ devices, and an average PCE of 14.2% on $FAPbI_3$ cells.

4.4. Rb+, Cs+, MA+, FA+ alloyed lead iodide for highly stable and efficient PSCs

So far, triple-cation (Cs+, MA+, FA+) perovskites exploited for use in photovoltaic applications have been processed based on proper sizes, relative compositions of cations and precise control of Br⁻ doping, as realized in $Cs_x(MA_{0.17}FA_{0.83})_{1-x}Pb(I_{0.83}Br_{0.17})_3$ settings [131], and mixed-cation MA+/FA+ systems in MAPbBr₃:FAPbI₃ or MABr:FAPbI₃, so as to reduce lattice strains for modified Goldschmidt tolerance factors for stable perovskites, as reported in works [66,69,102,132-134]. Nonetheless, Saliba et al. [130,135] showed that the incorporation of small-size Rb⁺ into the lattice of (Cs+,MA+,FA+)PbI₃ can achieve stable and efficient PSCs with stabilized output of PCE over 20% in long-term operations, without the necessary involvement of Br⁻. As shown in Fig. 18(a), cation-alloyed (Rb+,Cs+,MA+,FA+)PbI3 based solar cell exhibited a top 21.8% PCE with a $J_{\rm sc}$ of 22.8 mA cm⁻², $V_{\rm oc}$ of 1.18 V and FF of 0.81, while the inset accounts for time-dependent output of PCE at maximum power point of the device, with a 21.6% PCE,

 $0.977\,\mathrm{V}$ and $22.1\,\mathrm{mA}~\mathrm{cm}^{-2}$ stabilized by $60\,\mathrm{s}$ [130]. Likewise, V_{oc} was tracked with respect to time lapse on a device with greatest $V_{\rm oc}$, as shown in Fig. 18(b), where a $V_{\rm oc}$ of 1.24 V was stabilized by 120 s. Importantly, to test the robustness of optoelectronic structure and quantum efficiency of (Rb+,Cs+,MA+,FA+)PbI₃, which allowed efficient and reversible photon-electron conversion as previously realized in perovskite light-emitting diodes (LEDs) [136-143], electroluminescence (EL) was performed on the (Rb+,Cs+,MA+,FA+)PbI₃ device. As shown in Fig. 18(c), the EQE started to increase as applied voltage surpassed ~1.1 V and reached ~3.8% at 2.5 V, demonstrating a highest efficiency in the field of perovskite LEDs [130,141-143]. Meanwhile, inset EL spectrum and photograph showing a peak wavelength at ~760 nm and the red-emitting device, respectively. To validate the long-term stability of (Rb+,Cs+,MA+,FA+)PbI₃ based device, PCEs of the solar cell were recorded over a 500-hour duration, with the cell aged at 85 °C in nitrogen atmosphere and under constant light soaking, as shown in Fig. 18(d). Stunningly, after 500 h of aging, 95% of original performance could be retained, and therefore proved the exceptional operation stability.

4.5. Issues with Rb^+ , $C(NH_2)_3^+(GA^+)$ incorporation in perovskite

Doubt arises if Rb⁺ was truly incorporated into perovskite lattice due to its small ionic radius (152 pm) [144–146], as in the case of (Rb⁺,Cs⁺,MA⁺,FA⁺)PbI₃. We consider that, instead of occupying perovskite A-site nanoscopic voids, Rb⁺ rather intercalates at the interstices of perovskite lattices, as was claimed in previous report [147]. Such intercalations, because of inefficient

16

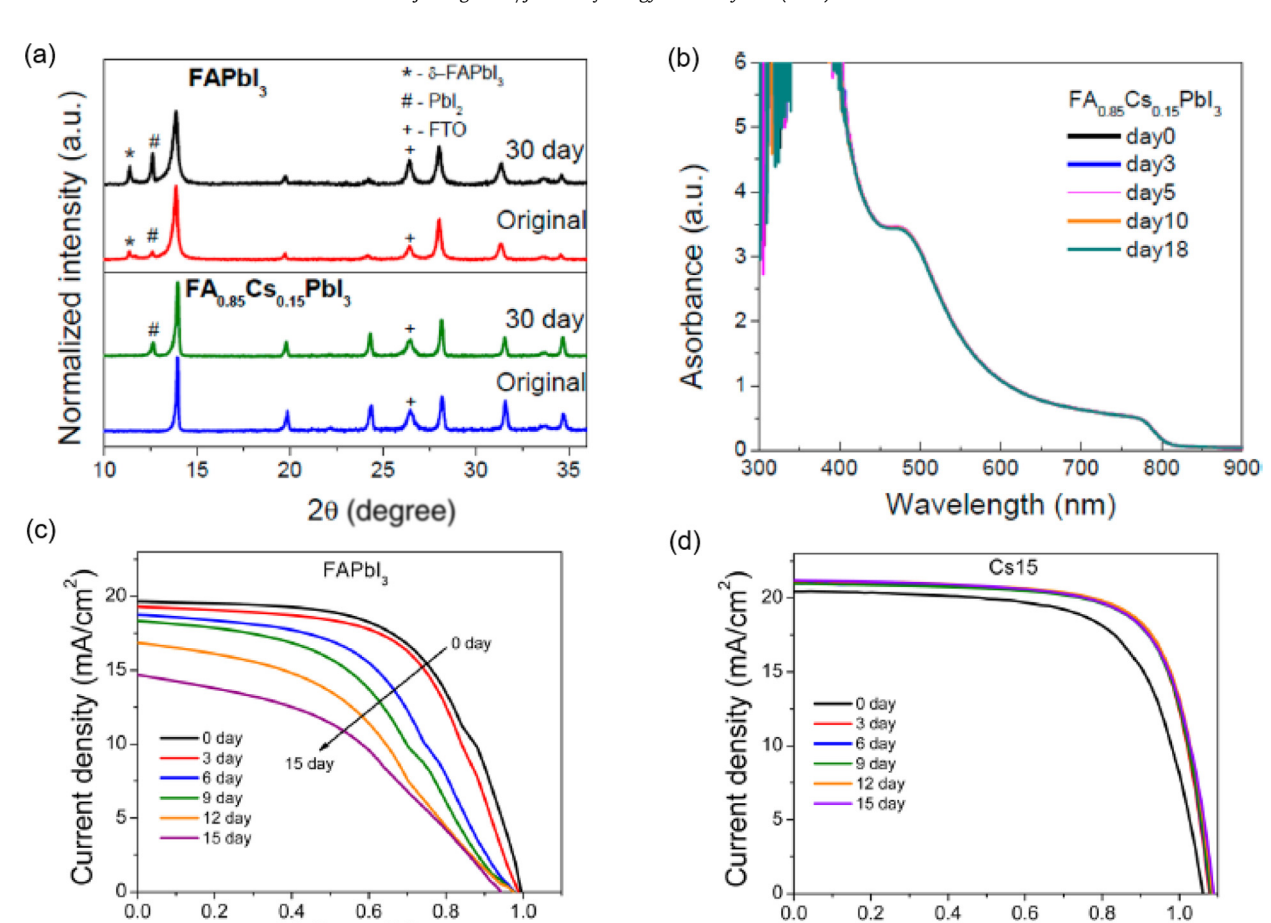


Fig. 17. Structural, optical and photovoltaic properties of FAPbl₃ and FA_{0.85}Cs_{0.15}Pbl₃ thin films [63]. (a) Comparison of XRD patterns of FA_{0.85}Cs_{0.15}Pbl₃ thin film after fabrication (blue), 30 days of aging in dry air (green) with FAPbl₃ thin film after fabrication (red), 30 days of aging in dry air (black), with *, # and + denoting structures of δ-FAPbl₃, Pbl₂ and FTO. (b) Evolution of UV-vis absorbance spectra of FA_{0.85}Cs_{0.15}Pbl₃ thin film from 0 day to 18 days of aging in dry air. (c,d) Evolution of J-V curves of pristine FAPbl₃, FA_{0.85}Cs_{0.15}Pbl₃ based solar cells from 0 day to 15 days of aging in dry air, respectively. © ACS. Reproduced with permission granted by ACS from ref. [63]. Permission to reuse must be obtained from the copyright holder.

Voltage (V)

Voltage (V)

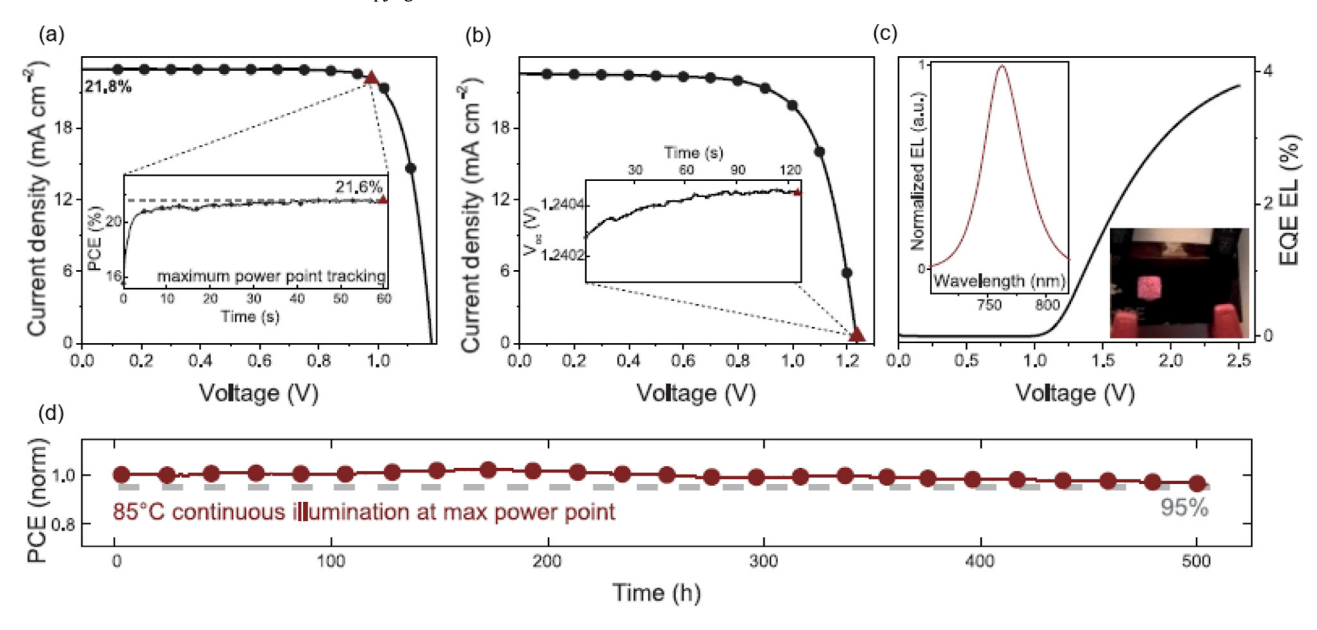


Fig. 18. Photovoltaic, electroluminescent and stability properties of $(Rb^+,Cs^+,MA^+,FA^+)Pbl_3$ based device [130]. (a) J-V curve of $(Rb^+,Cs^+,MA^+,FA^+)Pbl_3$ based solar cell with highest PCE of 21.8%, while inset shows time-dependent PCE with a 21.6% efficiency stabilized by 60s (indicated by red triangles). (b) J-V curve of mixed-cation device with highest V_{oc} , with inset showing time-dependent V_{oc} with 1.24V stabilized at the end of 120s (indicated by red triangles). (c) Voltage-dependent EL EQE curve with an onset voltage of ~1.1 V, with inset photograph being the light-emitting device and spectrum being EL spectrum with a peak wavelength at around 760 nm. (d) Stability test of mixed-cation $(Rb^+,Cs^+,MA^+,FA^+)Pbl_3$ device with 95% of original performance retained by 500 h of aging under constant AM1.5 G illumination at 85 °C in nitrogen atmosphere. © AAAS. Reprint with permission granted by AAAS from ref. [130]. Permission to reuse must be obtained from the copyright holder.



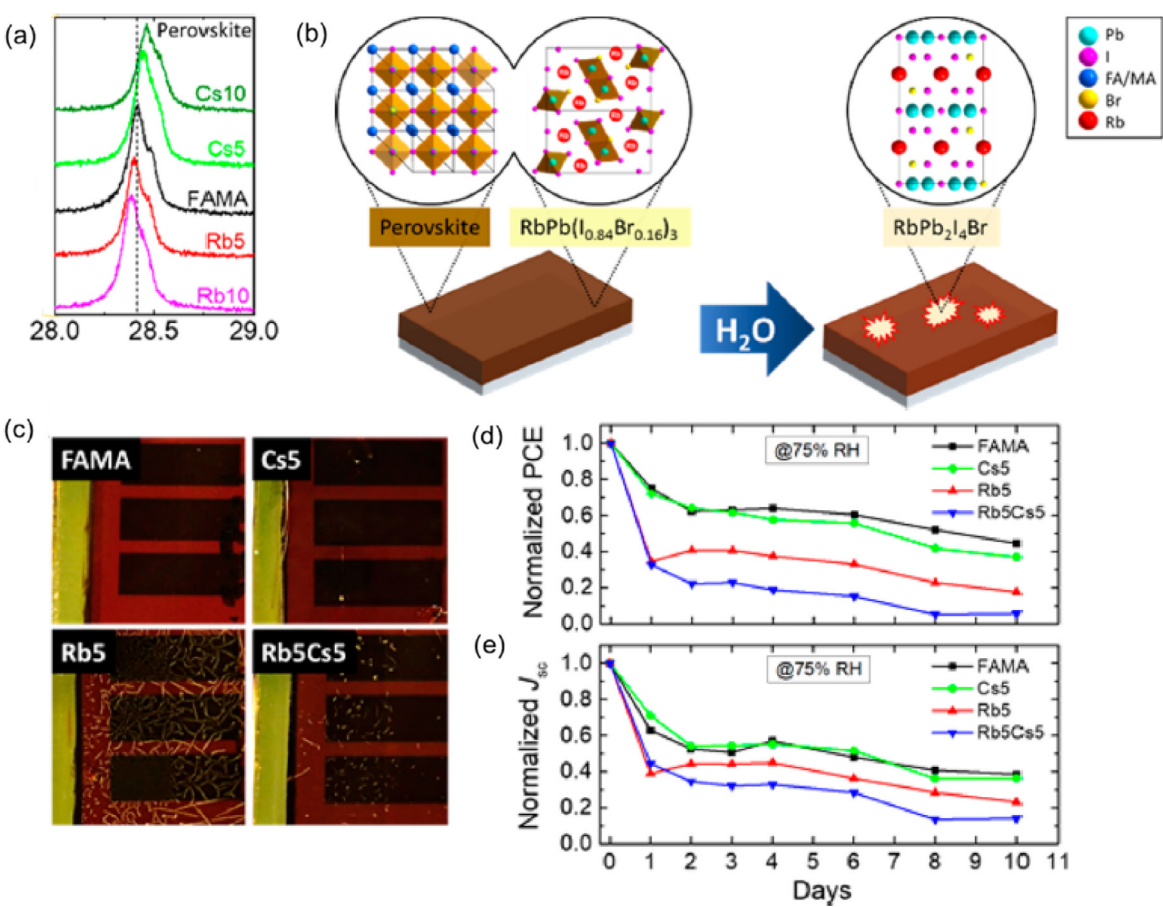


Fig. 19. Structural characteristics, degradation illustration and photovoltaic stabilities of Rb-containing mixed-cation/halide perovskites [146]. (a) Comparison of (220) planes on thin film $(FA_{0.83}MA_{0.17})_{0.95}Cs_{0.1}Pb(l_{0.83}Br_{0.17})_3$ (dark green), $(FA_{0.83}MA_{0.17})_{0.95}Cs_{0.05}Pb(l_{0.83}Br_{0.17})_3$ (green), $FA_{0.83}MA_{0.17}Pb(l_{0.83}Br_{0.17})_3$ (green), $FA_{0.83}MA_{0.17}Pb(l_{0.83}Br_{0.17})_3$ (green), $FA_{0.83}MA_{0.17}Pb(l_{0.83}Br_{0.17})_3$ (magenta). (b) Schematic illustration of phase separation and degradation of Rb-containing perovskite films. (c) Photographs of solar cell devices based on perovskites with different cation compositions over 10 days of aging in 75% RH in the air at RT under dark condition, respectively. © ACS. Reproduced with permission granted by ACS from ref. [146]. Permission to reuse must be obtained from the copyright holder.

atomic packing, subsequently led to expansion of material lattices [147], and is evidenced by XRD peaks that shift towards smaller 2θ angles with increasing Rb⁺ contents in FA/MA mixed-cation perovskite systems (Fig. 19a) [146]. On the contrary, Cs⁺ doping effectively results in smaller lattice spacing of material structures with greater cation concentrations, as indicated by the XRD peaks that shift towards larger 2θ angles (Fig. 19b) [146]. Therefore, Cs⁺ may be the "goldilocks" cation in terms of smallest ionic size that can be properly situating on the A-site lattice points. In fact, due to the homogeneous chemical environment caused by 100% composition I⁻ (r=220 pm) [130,146], the exact location or coordinative profiles of Rb+ with respect to inorganic PbI₃octahedral framework remains ambiguous, as in the practice of (Rb⁺,Cs⁺,MA⁺,FA⁺)PbI₃. However, it was this large lattice volume that accommodated Rb+ and prevented phase separation. In fact, in the presence of Br^- , as in the case of $FA_{0.83}MA_{0.17}Pb(I_{0.83}Br_{0.17})_3$, Rb⁺ tends to form non-perovskite structure RbPb(I_{0.84}Br_{0.16})₃, and therefore separates from bulk 3-D perovskite phase; moreover, under moisture effects, this Rb+/Br- containing phase favorably degrades into RbPb₂I₄Br, as illustrated in Fig. 19(b). Such Rb+/Br- induced phase separations and degradations can be directly perceived on the photographs of solar cell devices based on cation/anion alloyed $(FA_{0.83}MA_{0.17})_{0.95}Rb_{0.05}Pb(I_{0.83}Br_{0.17})_3$ and $(FA_{0.83}MA_{0.17})_{0.9}Cs_{0.05}Rb_{0.05}Pb(I_{0.83}Br_{0.17})_3$ systems, as shown in Fig. 19(c). Photovoltaically, due to the phase instability of Rb-containing perovskites, unencapsulated devices showed poor retention of orig-

inal PCE and J_{sc} across 10 days of aging in 75% relative humidity (RH) condition, when compared with FA_{0.83}MA_{0.17}Pb(I_{0.83}Br_{0.17})₃ and (FA_{0.83}MA_{0.17})_{0.95}Cs_{0.05}Pb(I_{0.83}Br_{0.17})₃ counterparts, as shown in Fig. 19(d) and (e).

To date, the incorporation of large-size GA⁺ (278 pm) [148–150] into perovskite lattices has not been clearly proved. Previously, De Marco and coworkers [150] found that MA⁺/GA⁺ cocationed lead iodide perovskite (composition ratio $MA^+/GA^+ = 6$) had a XRD pattern that is nearly the same with pristine MAPbI₃ thin film, as shown in Fig. 20(a). Supposedly, with such high concentration of large-size GA+doping (~14 mol%), obvious lattice expansion should be noticeably observed. The anomalous preservation of lattice spacing can only be explained by the GA⁺-structured side products that leach out of perovskite lattice when GA+ is low in concentration; and when GA+ has high composition ratios to MA⁺, total reformation of material structures may happen. In fact, as shown in Fig. 20(b), pure GAPbI₃ (100 mol,% GA⁺) displayed a diffraction pattern free of characteristic (110) and (220) perovskite structures, which therefore indicated the formation of non-perovskite materials. The non-perovskite structures of GAPbI₃ can be easily rationalized through the large Goldschmidt tolerance factor (t > 1.0), as calculated with ionic radii of Pb²⁺(119 pm or 133 pm) and I⁻ (220 pm or 203 pm) [76,130,151]. Nevertheless, by closely examining the crystal structure of GAPbI3, Dimesso et al. [152] discovered that pristine GAPbI₃ does not assume a single phase, and instead, both hexagonal and orthorhombic structures J. Gong et al./Journal of Energy Chemistry 000 (2018) 1-23

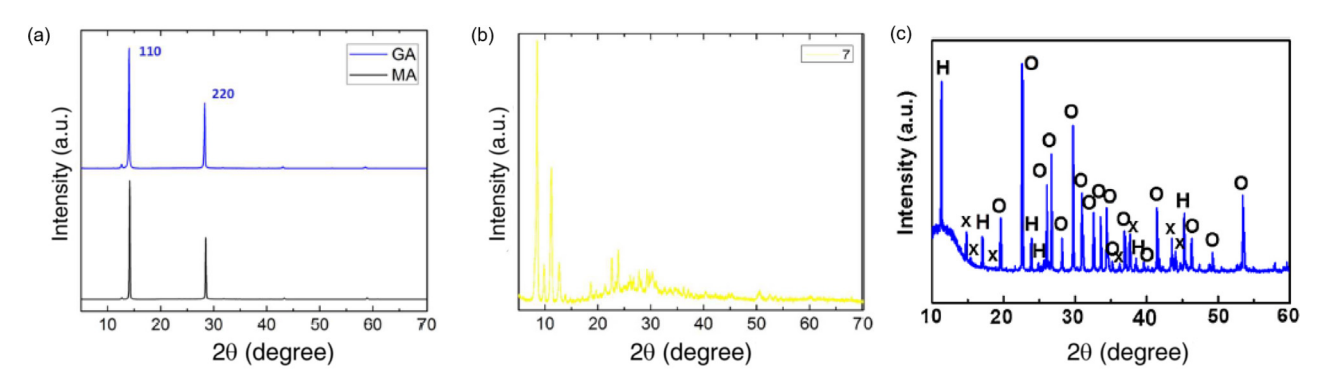


Fig. 20. Structural characterizations of $MA_{1-x}GA_xPbI_3$ thin films. (a) XRD patterns of $GA_{0.14}MA_{0.86}PbI_3$ thin film (blue), pristine MAPbI₃ thin film (black). (b) XRD pattern of pure GAPbI₃ thin film. © ACS. Reprint with permission granted by ACS from ref. [150]. (c) Indexed XRD pattern of GAPbI₃ thin film, where orthorhombic ("0"), hexagonal ("H") phases and unreacted guanidinium iodide ("x") were shown. © Elsevier. Reprint with permission granted by Elsevier from ref [152]. Permission to reuse must be obtained from the corresponding copyright holders.

simultaneously exist (Fig. 20c). This splitting of crystallographic symmetries in GAPbI₃ system directly contradicts the theoretically predicted hexagonal phase that corresponds to $t > 1.0 \, [63,130]$, and may in some way addresses the complex lattice structure as severely disrupted by oversized GA⁺ [150].

18

5. 2-D Ruddelsden-Popper layered perovskites for efficient and stable solar cells

5.1. Out-of-plane crystallographic alignment of $(BA)_2(MA)_3Pb_4I_{13}$

Stoumpos et al. [54,153] previously reported synthesis of a class of 2-D Ruddlesden-Popper type layered perovskites $(BA)_2(MA)_{n-1}Pb_nI_{3n+1}$ (n = 1, 2, 3, 4, 5, ∞), where the relative ratio of BA⁺ and MA⁺ was chemically adjusted to control the number of inorganic layers within each perovskite fragment, with BA+ served as spacer cations of inorganic fragments. Structurally, as *n* becomes larger, the resultant 2-D perovskite is optoelectronically resembling the 3-D MAPbI₃ counterpart due to increased dielectric screening and mitigated quantum confinement effects [153-155]. For example, $(BA)_2(MA)_3Pb_4I_{13}$ (n=4, structure shown in Fig. 21a) has a relatively small bandgap (\sim 1.90 eV) and an $E_{\rm b}$ smaller than 1 eV, contrasting with $\sim\!\!1.50\,\mathrm{eV}$ of E_g and an E_b smaller than 10 meV on $MAPbI_3$ [15,59,124,153,156,157]. Different from single-layer (n = 1) $(MA)_2Pb(SCN)_2I_2$ 2-D perovskite that has also attracted multitude of attention, $(BA)_2(MA)_{n-1}Pb_nI_{3n+1}$ 2-D homologues are moisture stable with their relatively non-polar spacing BA⁺ cations [158]; they are also thermally stable which enables repeatable, convenient and large-scale fabrication of pure materials with simple solution methods [153]. Distinctively, what comes with the neat solution synthesis of the $(BA)_2(MA)_{n-1}Pb_nI_{3n+1}$ homologues are the strongly preferred crystallographic orientations of deposited materials, which gave rise to inorganic $[Pb_nI_{3n+1}]^{(n+1)}$ -fragments perpendicular to substrates and thus favoring efficient charge transport in solar cell applications [54,153]. Tsai and coworkers previously demonstrated that (BA)₂(MA)₃Pb₄I₁₃ thin films can be deposited on substrates with characteristic out-of-plane crystallinity through RT-cast and HT-cast methods that do not require thermal annealing [52], as proved by grazing incidence X-ray diffraction (GIXRD) patterns and grazing incidence wide-angle X-ray scattering (GIWAXS) image that are shown in Fig. 21(b) and (c), respectively. GIXRD pattern and GIWAXS image both confirmed the prominent existence of (111) and (202) planes in HT-cast (BA)₂(MA)₃Pb₄I₁₃ thin films, where GIWAXS map spectrally revealed ($\bar{1}1\bar{1}$), ($\bar{1}11$) and ($\bar{2}02$) orientations. The appearance of crystallographic planes at specific GIWAXS vector positions comprehensively indicated an out-of-plane alignment of (BA)₂(MA)₃Pb₄I₁₃

crystal structure with respect to underlying substrate, as shown in Fig. 21(d). Such out-of-plane (BA)₂(MA)₃Pb₄I₁₃ crystalline eventually led to a top PCE of 12.52% with $J_{\rm sc}$ of \sim 16 mA cm $^{-2}$ and $V_{\rm oc}$ of $\sim 0.9 \, \text{V}$ in solar cells fabricated with HT-cast method, as derived from J-V curves shown in Fig. 21(e). Remarkably, no hysteresis was witnessed between forward and reverse voltage scans, which could be explained by the greatly reduced trap states and depleted charge accumulation zone in the device [52]. Stability tests indicated that unencapsulated (BA)₂(MA)₃Pb₄I₁₃ device retained more than 60% of original PCE by 2250 h of constant AM1.5 G illumination, while unencapsulated MAPbI3 cell almost lost all the photovoltaic performance after 2250 h of constant AM1.5 G illumination, as shown in Fig. 21(f). As for encapsulated devices and shown in Fig. 21(h), $(BA)_2(MA)_3Pb_4I_{13}$ based cell reached ~110% of original performance by 2750h of continuous illumination, but the PCE on MAPbI₃ cell dropped drastically to ~10% of original performance by 2750h of light soaking, and therefore signified a weak photostability on 3-D perovskite material. Significantly, as shown in Fig. 21(g), unencapculated MAPbI₃ device nearly lost all the photoconversion efficiency by ~10 h of aging under 65% RH, but unencapsulated (BA)₂(MA)₃Pb₄I₁₃ based device could maintain \sim 20% of original PCE by \sim 25 h of aging under 65% RH. The enhanced moisture stability of (BA)2(MA)3Pb4I13 when contrasted with MAPbI₃ was more apparent on encapsulated devices. As shown in Fig. 21(i), encapsulated (BA)₂(MA)₃Pb₄I₁₃ cell retained \sim 80% of original PCE by \sim 2100 h of aging under 65% RH, while PCE of MAPbI₃ cell dropped drastically to ~10% by 500 h of humidity

5.2. Polymer ammonium (PEI+)/MA+mixed-cation 2-D layered perovskites

When the spacer cations in mixed-cation 2-D lead iodide perovskites were taken to an extreme—long chain PEI⁺, the humidity stability of resultant perovskites can be further enhanced when compared with $(BA)_2(MA)_{n-1}Pb_nI_{3n+1}$ because of strongly hydrophobic PEI⁺, as previously demonstrated by Yao et al. [159,160], where the structure of PEI⁺ and humidity stabilities of $(PEI)_2(MA)_{n-1}Pb_nI_{3n+1}$ (n=3, 5, 7) thin films are shown in Fig. 22(a) and (b), respectively. To determine the crystal structures of $(PEI)_2(MA)_{n-1}Pb_nI_{3n+1}$ 2-D perovskites, XRD was performed on $(PEI)_2(MA)_2Pb_3I_{10}$, $(PEI)_2(MA)_4Pb_5I_{16}$ and $(PEI)_2(MA)_6Pb_7I_{22}$ powders, as shown in left portion of Fig. 22(c), and their structures were unambiguously configured to be n-1 layers of $[Pb_nI_{3n+1}]^{(n+1)-}$ inorganic fragments spaced by in-plane oriented PEI⁺ cations relative to (0k0) alignments, as shown in right part of Fig. 22(c). Notably, while being structurally similar

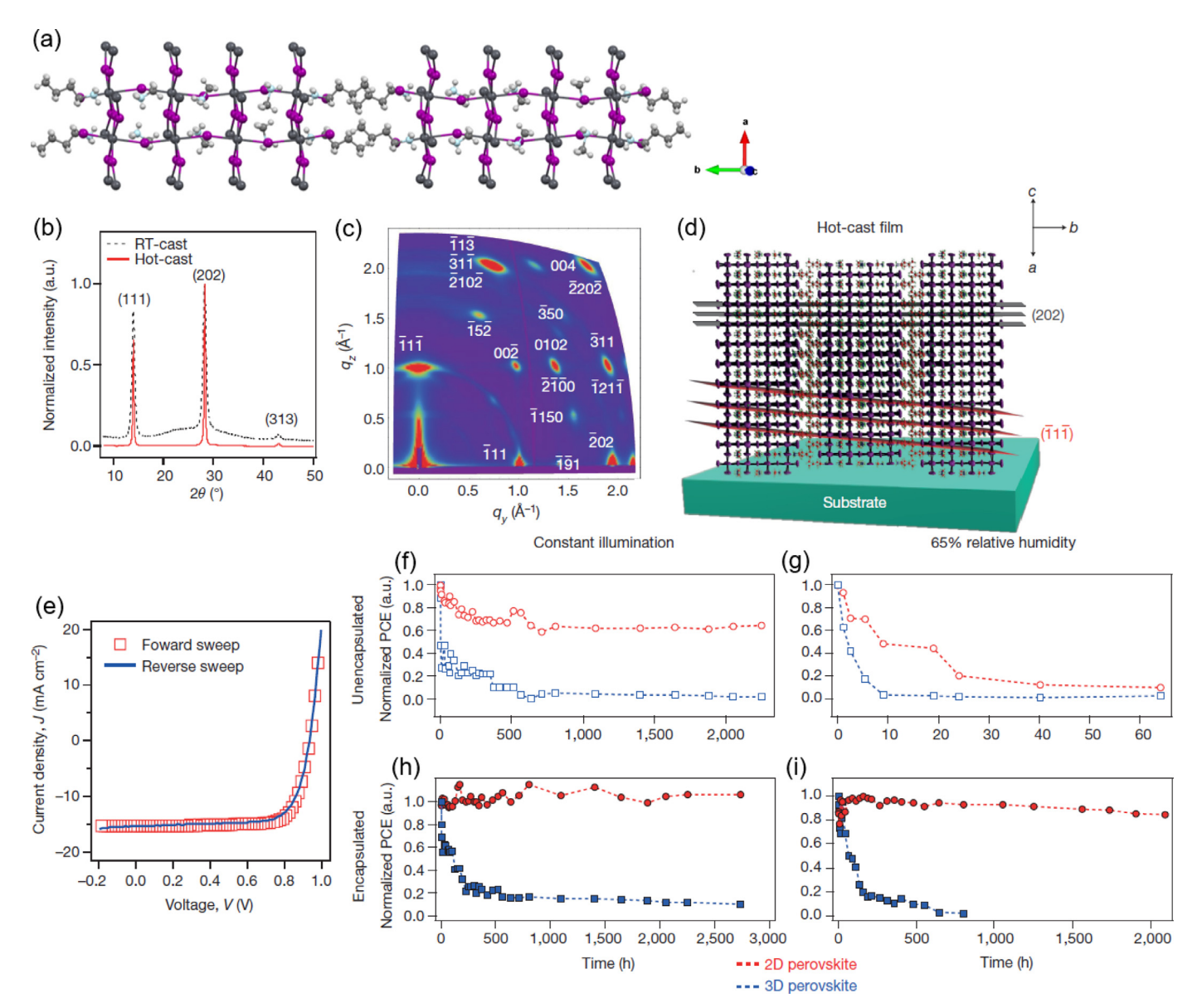


Fig. 21. Structural, photovoltaic and stability characterizations of (BA)₂(MA)₃Pb₄I₁₃. (a) Crystal structure of (BA)₂(MA)₃Pb₄I₁₃, as viewed from (001) direction. Structure was reconstructed with cif file from work [153]. (b) GIXRD spectra of (BA)₂(MA)₃Pb₄I₁₃ films deposited via RT-cast method (dashed), HT-cast method (red), with HT-cast method resulting in (BA)₂(MA)₃Pb₄I₁₃ 2-D perovskite with higher crystallinity [52]. (c) GIWAXS map of HT-cast (BA)₂(MA)₃Pb₄I₁₃ film. Presence of zone-like intensities indicates high crystallinity of (BA)₂(MA)₃Pb₄I₁₃ film [52]. (d) Schematic illustration of orientation-resolved (BA)₂(MA)₃Pb₄I₁₃ on underlying substrate from (101) direction, showing (111) and (202) planes [52]. (e) Hysteresis-free J–V curves of HT-cast (BA)₂(MA)₃Pb₄I₁₃ based solar cell, with forward scan and reverse scan shown in red squares and blue line, respectively [52]. (f,h) Time-dependent normalized PCE of MAPbI₃ (blue) and (BA)₂(MA)₃Pb₄I₁₃ (red) based devices without encapsulation, with encapsulation, respectively, under constant AM1.5 G illumination [52]. (g,i) Time-dependent normalized PCE of MAPbI₃ (blue) and (BA)₂(MA)₃Pb₄I₁₃ (red) based devices without encapsulation, with encapsulation, respectively, under constant 65% RH condition [52]. © Nature Publishing Group (NPG). Reprint with permission granted by NPG from ref. [52]. Permission to reuse must be obtained from the copyright holder.

to $(BA)_2(MA)_{n-1}Pb_nI_{3n+1}$ systems reported by Stoumpos et al. [52,54,153], the orientation of organic cations PEI⁺ was horizontal with respect to the ac-direction of $[Pb_nI_{3n+1}]^{(n+1)-}$ octahedral framework, thereby pointing the side-chain cationic ammonium groups directly toward the terminal ends of $[Pb_nI_{3n+1}]^{(n+1)-}$ anionic fragments and contributing to a strengthened electrostatic interaction between cationic and anionic sublattices. Moreover, just like $(BA)_2(MA)_{n-1}Pb_nI_{3n+1}$ 2-D perovskites, these $(PEI)_2(MA)_{n-1}Pb_nI_{3n+1}$ systems were spun coated from solutions to form high-quality, vertically grown phases on underlying substrates in facile kinetics [160], and therefore exhibited phenomenal photovoltaic properties on fabricated solar cell devices with small (0.04 cm^2) and large (2.32 cm^2) active areas, as shown in Fig. 22(d) and (e), respectively. $(PEI)_2(MA)_2Pb_3I_{10}$, $(PEI)_2(MA)_4Pb_5I_{16}$

and (PEI)₂(MA)₆Pb₇I₂₂ based small-area devices showed maximum PCEs as 4.81%, 7.63% and 10.08%, while MAPbI₃ small-area cell fabricated with solvent engineering (MAPbI₃ (M)) method achieved top PCE as 15.42%. It was clear that solar cell performance in (PEI)₂(MA)_{n-1}Pb_nI_{3n+1} devices was monotonically improved as n increased, which was due to the progressive narrowing of optical bandgaps, reduction of exciton binding energies along with increased layer thickness (n-1) of inorganic fragments that facilitated greater probability of ac-plane charge transport, which was not hindered by PEI⁺ spacers [160–162]. The narrowing of (PEI)₂(MA)_{n-1}Pb_nI_{3n+1} optical bandgaps as n enlarged was echoed with monotonic increases in average J_{sc} as 6.63 mA cm⁻², 10.22 mA cm⁻² and 13.12 mA cm⁻², decreases in average V_{oc} as 1.21 V, 1.16 V and 1.10 V on (PEI)₂(MA)₂Pb₃I₁₀, (PEI)₂(MA)₄Pb₅I₁₆



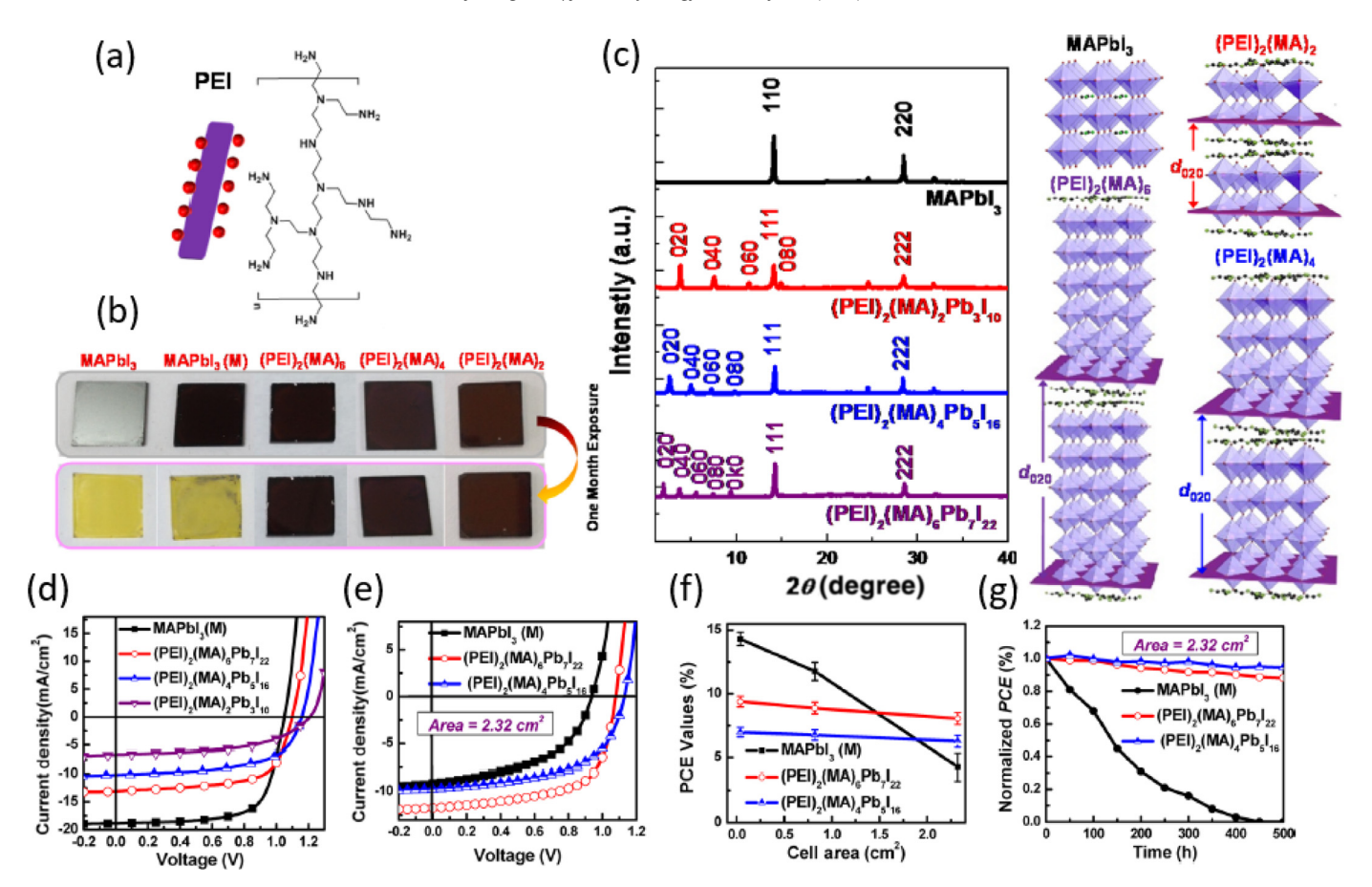


Fig. 22. Structural, stability and photovoltaic properties of $(PEI)_2(MA)_{n-1}Pb_nI_{3n+1}$ [160]. (a) Structure of PEI+, with red spheres of schematic representation indicating ammonium sides of polymer cation. (b) From left to right: photographs of thin film-MAPbI₃ deposited from simple one-step process, MAPbI₃ fabricated with solvent engineering, $(PEI)_2(MA)_6Pb_7I_{22}$, $(PEI)_2(MA)_4Pb_5I_{16}$ and $(PEI)_2(MA)_2Pb_3I_{10}$. Top: as-synthesized films; bottom: corresponding films after a month of aging in 50% RH. (c) XRD patterns (left) of powder MAPbI₃ (black), $(PEI)_2(MA)_2Pb_3I_{10}$ (red), $(PEI)_2(MA)_4Pb_5I_{16}$ (blue) and $(PEI)_2(MA)_6Pb_7I_{22}$ (purple), and corresponding schematic illustration of resolved crystal structures (right) with (020) planes marked. (d) J-V curves of solar cells with active area of 0.04 cm² based on MAPbI₃ (black), $(PEI)_2(MA)_6Pb_7I_{22}$ (red), $(PEI)_2(MA)_4Pb_5I_{16}$ (blue) and $(PEI)_2(MA)_6Pb_7I_{22}$ devices with 2.32 cm² active area, respectively. (f) Active area-dependent performance of solar cells based on MAPbI₃ (black), $(PEI)_2(MA)_4Pb_5I_{16}$ (blue) and $(PEI)_2(MA)_6Pb_7I_{22}$. © ACS. Reprint with permission granted by ACS from ref. [160]. Permission to reuse must be obtained from the copyright holder.

and (PEI)₂(MA)₆Pb₇I₂₂ devices with small active areas, respectively. However, it is well known that small active areas on perovskite solar cells may not reflect the real J-V properties of scale-up devices by overlooking many factors such as measurement errors, trap states and inhomogeneity of perovskite morphology [8,160,163–166]. Therefore, large-area $(PEI)_2(MA)_{n-1}Pb_nI_{3n+1}$ based solar cells were fabricated, and maximum PCEs were achieved as 6.99% and 8.77% on $(PEI)_2(MA)_4Pb_5I_{16}$ and $(PEI)_2(MA)_6Pb_7I_{22}$ devices, respectively, contrasting with top PCE of 5.82% on MAPbI₃ (M) device. The superior performance on (PEI)₂(MA)₄Pb₅I₁₆ and (PEI)₂(MA)₆Pb₇I₂₂ large-area devices with respect to prototypical MAPbI₃ (M) large-area device indicated the high uniformity and extremely low trap state densities within 2-D perovskites. In fact, enlargement in cell active area had a significantly larger negative impact of solar cell performance on MAPbI₃ (M) device than $(PEI)_2(MA)_4Pb_5I_{16}$ and $(PEI)_2(MA)_6Pb_7I_{22}$ devices, as illustrated in Fig. 22(f). The non-polar nature of PEI+ induced outstanding stabilities on 2-D (PEI)₂(MA)₄Pb₅I₁₆ and (PEI)₂(MA)₆Pb₇I₂₂, which was indicated through unencapsulated solar cell stability tests as shown in Fig. 22(g), where PCE of MAPbI₃ (M) dropped dramatically below 20% of original performance after 300 h of aging while $(PEI)_2(MA)_6Pb_7I_{22}$ and $(PEI)_2(MA)_4Pb_5I_{16}$ devices retained ${\sim}90\%$ of original PCE by 500 h of aging.

6. Conclusions and future research directions

Long-chain cationic ligands (such as oleylammonium, phenylethylammonium) are able to stabilize α -CsPbI₃ and α -FAPbI $_3$ nanostructures through surface functionalization at ambient conditions, and formidable photovoltaic performance was achieved on solar cell devices based on stabilized α -CsPbI₃ and α -FAPbI₃ nanocrystals. Novelly, sulfobetaine zwitterions were applied to successfully stabilize perovskite α -CsPbI₃ and achieved formidable and stable solar cell performance. Since Goldschmidt tolerance factors were tuned with different sizes of cations in (MA,FA)PbI₃, (Cs,FA)PbI₃, (Rb,Cs,MA,FA)PbI₃ alloyed perovskites, chemically stable black-phase materials were achieved with phenomenal photovoltaic properties. Through occupying A-site lattice points, incorporation of Cs+ enhanced thermal stability and carrier lifetimes of hybrid perovskite, as proved in the case of MA_{0.95}Cs_{0.05}PbI₃, while Rb⁺/Br⁻-containing perovskites exhibited significant degradation through moisture aging and intrinsic phase separation. With the large ionic radius (278 pm), the incorporation of GA+ into perovskite lattice still has not been clearly proved. Due to the low polarities of long alkyl chains, (BA)₂(MA)₃Pb₄I₁₃ and $(PEI)_2(MA)_{n-1}Pb_nI_{3n+1}$ 2-D layered perovskites had high moisture stabilities and thus stable photovoltaic performance. With proper

encapsulation, PSCs based on these photoactive materials had durable performance under constant AM1.5 G illumination or high RH conditions up to hundreds of hours. Stunningly, α -FAPbl $_3$ based solar cell devices, as fabricated by Yang et al. [66] and Zhou et al. [75], were hysteresis-free due to the lack of MA $^+$ [167] and greatly annihilated trap states in perovskite layers with high-quality morphologies. As for (BA) $_2$ (MA) $_3$ Pb $_4$ I $_1$ 3 devices reported by Tsai et al. [52], lack of trap states as well as efficient charge extraction were responsible for hysteresis-free behavior of solar cell performance.

While α -CsPbI₃ and α -FAPbI₃ were successfully stabilized with surface ligand functionalization and achieved good photovoltaic performance on solar cells, we believe these nanostructures will find major applications as optoelectronics in the future, such as light-emitting diodes, photodetectors and lasers, due to their tunable material bandgaps, as already achieved in works [168-177]. Additionally, according to the anion exchange reactions that were previously practiced to grow perovskite nanostructures [178,179], it is potentially viable to synthesize lead-free perovskites through cation exchanges. Moreover, as the mixed-cation (Rb,Cs,MA,FA)PbI₃ alloyed perovskites achieved PCE above ~20%, research in optimizing the relative cation contents, as coupled with chemical pathways that improved the processing of perovskite layers, will be continued to further boost up solar cell performance. Thermal annealing steps were not necessary in the fabrications of $(BA)_2(MA)_{n-1}Pb_nI_{3n+1}$ and $(PEI)_2(MA)_{n-1}Pb_nI_{3n+1}$ thin films, and thus indicating the small thermodynamic differences between solid and solution-equilibrated phases of the 2-D materials [52,160]. Furthermore, due to the structural versatility of polymer chains, customized polymeric ammonium cations with tailored functional groups will be employed to invent different 2-D layered perovskites with new material properties.

Acknowledgments

T.X. acknowledges financial support from the U.S. National Science Foundation (CBET-1150617). S.E.B. and G.V.P. acknowledge financial support from the U.S. National Science Foundation REU Grant (CHE-1659548). Use of the Center for Nanoscale Materials, an Office of Science user facility, was supported by the U.S. Department of Energy, Office of Science, Office of Basic Energy Sciences, under Contract No. DE-AC02-06CH11357.

References

- [1] A. Kojima, K. Teshima, Y. Shirai, T. Miyasaka, J. Am. Chem. Soc. 131 (17) (2009) 6050–6051.
- [2] National Renewable Energy Laboratory, Best Research-Cell Efficiencies, NREL Research Cell Efficiency Records, National Renewable Energy Laboratory, Golden, CO, 2017 Available at https://www.nrel.gov/pv/assets/images/ efficiency-chart.png accessed 09.06.2017.
- [3] J. Burschka, N. Pellet, S.-J. Moon, R. Humphry-Baker, P. Gao, M.K. Nazeeruddin, M. Gratzel, Nature 499 (2013) 316–319.
- [4] J.-H. Im, I.-H. Jang, N. Pellet, M. Gratzel, N.-G. Park, Nat. Nanotechnol. 9 (2014) 927–932.
- [5] M. Kaltenbrunner, G. Adam, E.D. Glowacki, M. Drack, R. Schwodiauer, L. Leonat, D.H. Apaydin, H. Groiss, M.C. Scharber, M.S. White, N.S. Sariciftci, S. Bauer, Nat. Mater. 14 (2015) 1032–1039.
- [6] M.A. Green, A. Ho-Baillie, H.J. Snaith, Nat. Photon. 8 (2014) 506-514.
- [7] W. Nie, H. Tsai, R. Asadpour, J.-C. Blancon, A.J. Neukirch, G. Gupta, J.J. Crochet, M. Chhowalla, S. Tretiak, M.A. Alam, H.-L. Wang, A.D. Mohite, Science 347 (6221) (2015) 522–525.
- [8] W. Chen, Y. Wu, Y. Yue, J. Liu, W. Zhang, X. Yang, H. Chen, E. Bi, I. Ashraful, M. Gratzel, L. Han, Science 350 (6263) (2015) 944–948.
- [9] J.H. Noh, S.H. Im, J.H. Heo, T.N. Mandal, S.I. Seok, Nano Lett. 13 (4) (2013) 1764–1769.
- [10] Y. Chen, H.T. Yi, X. Wu, R. Haroldson, Y.N. Gartstein, Y.I. Rodionov, K.S. Tikhonov, A. Zakhidov, X.-Y. Zhu, V. Podzorov, Nat. Commun. 7 (2016) 12253.
- [11] D. Shi, V. Adinolfi, R. Comin, M. Yuan, E. Alarousu, A. Buin, Y. Chen, S. Hoogland, A. Rothenberger, K. Katsiev, Y. Losovyj, X. Zhang, P.A. Dowben, O.F. Mohammed, E.H. Sargent, O.M. Bakr, Science 347 (6221) (2015) 519–522.
- [12] S.D. Stranks, G.E. Eperon, G. Grancini, C. Menelaou, M.J.P. Alcocer, T. Leijtens, L.M. Herz, A. Petrozza, H.J. Snaith, Science 342 (6156) (2013) 341–344.

- [13] G. Xing, N. Mathews, S. Sun, S.S. Lim, Y.M. Lam, M. Gratzel, S. Mhaisalkar, T.C. Sum, Science 342 (6156) (2013) 344–347.
- [14] C. Wehrenfennig, G.E. Eperon, M.B. Johnston, H.J. Snaith, L.M. Herz, Adv. Mater. 26 (10) (2014) 1584–1589.
- [15] A. Miyata, A. Mitioglu, P. Plochocka, O. Portugall, J.T.-W. Wang, S.D. Stranks, H.J. Snaith, R.J. Nicholas, Nat. Phys. 11 (2015) 582–587.
- [16] V. D'Innocenzo, G. Grancini, M.J.P. Alcocer, A.R.S. Kandada, S.D. Stranks, M.M. Lee, G. Lanzani, H.J. Snaith, A. Petrozza, Nat. Commun. 5 (2014) 3586.
- [17] Q. Lin, A. Armin, R.C.R. Nagiri, P.L. Burn, P. Meredith, Nat. Photon. 9 (2015) 106–112
- [18] J. Even, L. Pedesseau, C. Katan, J. Phys. Chem. C 118 (22) (2014) 11566–11572.
- [19] Y. Yamada, T. Nakamura, M. Endo, A. Wakamiya, Y. Kanemitsu, IEEE J. Photo-volt. 5 (1) (2015) 401–405.
- [20] N.J. Jeon, J.H. Noh, Y.C. Kim, W.S. Yang, S. Ryu, S.I. Seok, Nat. Mater. 13 (2014) 897–903.
- [21] C. Eames, J.M. Frost, P.R.F. Barnes, B.C. O'Regan, A. Walsh, M.S. Islam, Nat. Commun. 6 (2015) 7497.
- [22] T.M. Brenner, D.A. Egger, L. Kronik, G. Hodes, D. Cahen, Nat. Rev. Mater. 1 (2016) 15007.
- [23] H. Zhu, K. Miyata, Y. Fu, J. Wang, P.P. Joshi, D. Niesner, K.W. Williams, S. Jin, X.-Y. Zhu, Science 353 (6306) (2016) 1409–1413.
- [24] J. Gong, M. Yang, X. Ma, R.D. Schaller, G. Liu, L. Kong, Y. Yang, M.C. Beard, M. Lesslie, Y. Dai, B. Huang, K. Zhu, T. Xu, J. Phys. Chem. Lett. 7 (15) (2016) 2879–2887.
- [25] X.-Y. Zhu, V. Podzorov, J. Phys. Chem. Lett. 6 (23) (2015) 4758–4761.
- [26] M. Park, N. Kornienko, S.E. Reyes-Lillo, M. Lai, J.B. Neaton, P. Yang, R.A. Mathies, Nano Lett. 17 (7) (2017) 4151–4157.
- [27] G. Grancini, C. Roldan-Carmona, I. Zimmermann, E. Mosconi, X. Lee, D. Martineau, S. Narbey, F. Oswald, F. De Angelis, M. Graetzel, M.K. Nazeeruddin, Nat. Commun. 8 (2017) 15684.
- [28] S. Yang, Y. Wang, P. Liu, Y.-B. Cheng, H.J. Zhao, H.G. Yang, Nat. Energy 1 (2016) 15016.
- [29] Y. Bai, Q. Dong, Y. Shao, Y. Deng, Q. Wang, L. Shen, D. Wang, W. Wei, J. Huang, Nat. Commun. 7 (2016) 12806.
- [30] Y. Rong, X. Hou, Y. Hu, A. Mei, L. Liu, P. Wang, H. Han, Nat. Commun. 8 (2017) 14555.
- [31] Y. Yang, J. You, Nature 544 (2017) 155-156.
- [32] J. You, L. Meng, T.-B. Song, T.-F. Guo, Y.M. Yang, W.-H. Chang, Z. Hong, H. Chen, H. Zhou, Q. Chen, Y. Liu, N. De Marco, Y. Yang, Nat. Nanotechnol. 11 (2016) 75–81.
- [33] X. Li, M.I. Dar, C. Yi, J. Luo, M. Tschumi, S.M. Zakeeruddin, M.K. Nazeeruddin, H. Han, M. Gratzel, Nat. Chem. 7 (2015) 703–711.
- [34] M. Gratzel, Nat. Mater. 13 (2014) 838-842.
- [35] J.M. Frost, K.T. Butler, F. Brivio, C.H. Hendon, M. van Schilfgaarde, A. Walsh, Nano Lett. 14 (5) (2014) 2584–2590.
- [36] A.M.A. Leguy, Y. Hu, M. Campoy-Quiles, M.I. Alonso, O.J. Weber, P. Azarhoosh, M. van Schilfgaarde, M.T. Weller, T. Bein, J. Nelson, P. Docampo, P.R.F. Barnes, Chem. Mater. 27 (9) (2015) 3397–3407.
- [37] I. Hwang, I. Jeong, J. Lee, M.J. Ko, K. Yong, ACS Appl. Mater. Interfaces 7 (31) (2015) 17330–17336.
- [38] G. Niu, X. Guo, L. Wang, J. Mater. Chem. A 3 (2015) 8970-8980.
- [39] G. Divitini, S. Cacovich, F. Matteocci, L. Cina, A. Di Carlo, C. Ducati, Nat. Energy 1 (2016) 15012.
- [40] N.-K. Kim, Y.H. Min, S. Noh, E. Cho, G. Jeong, M. Joo, S.-W. Ahn, J.S. Lee, S. Kim, K. Ihm, H. Ahn, Y. Kang, H.-S. Lee, D. Kim, Sci. Rep. 7 (2017) 4645.
- [41] E.J. Juarez-Perez, Z. Hawash, S.R. Raga, L.K. Ono, Y. Qi, Energy Environ. Sci. 9 (2016) 3406.
- [42] B. Brunetti, C. Cavallo, A. Ciccioli, G. Gigli, A. Latini, Sci. Rep. 6 (2016) 31896.
- [43] A. Dualeh, P. Gao, S.I. Seok, M.K. Nazeeruddin, M. Gratzel, Chem. Mater. 26 (21) (2014) 6160–6164.
- [44] S. Meloni, T. Moehl, W. Tress, M. Franckevicius, M. Saliba, Y.H. Lee, P. Gao, M.K. Nazeeruddin, S.M. Zakeeruddin, U. Rothlisberger, M. Graetzel, Nat. Commun. 7 (2016) 10334.
- [45] J. Xu, A. Buin, A.H. Ip, W. Li, O. Voznyy, R. Comin, M. Yuan, S. Jeon, Z. Ning, J.J. McDowell, P. Kanjanaboos, J.-P. Sun, X. Lan, L.N. Quan, D.H. Kim, I.G. Hill, P. Maksymovych, E.H. Sargent, Nat. Commun. 6 (2015) 7081.
- [46] M.D. McGehee, Nat. Mater. 13 (2014) 845–846.
- [47] B. Chen, M. Yang, S. Priya, K. Zhu, J. Phys. Chem. Lett. 7 (5) (2016) 905–917.
- [48] Q. Jiang, D. Rebollar, J. Gong, E.L. Piacentino, C. Zheng, T. Xu, Angew. Chem. Int. Ed. 54 (2015) 7617–7620.
- [49] Q. Tai, P. You, H. Sang, Z. Liu, C. Hu, H.L.W. Chan, F. Yan, Nat. Commun. 7 (2016) 11105.
- [50] X. Li, M.I. Dar, C. Yi, J. Luo, M. Tschumi, S.M. Zakeeruddin, M.K. Nazeeruddin, H. Han, M. Gratzel, Nat. Chem. 7 (2015) 703-711.
- [51] M. Daub, H. Hillebrecht, Angew. Chem. Int. Ed. 54 (38) (2015) 11016–11017.[52] H. Tsai, W. Nie, J.-C. Blancon, C.C. Stoumpos, R. Asadpour, B. Harutyun-
- yan, A.J. Neukirch, R. Verduzco, J.J. Crochet, S. Tretiak, L. Pedesseau, J. Even, M.A. Alam, G. Gupta, J. Lou, P.M. Ajayan, M.J. Bedzyk, M.G. Kanatzidis, A.D. Mohite, Nature 536 (2016) 312–316.
- [53] I.C. Smith, E.T. Hoke, D. Solis-İbarra, M.D. McGehee, H.I. Karunadasa, Angew. Chem. Int. Ed. 53 (42) (2014) 11232–11235.
- [54] D.H. Cao, C.C. Stoumpos, O.K. Farha, J.T. Hupp, M.G. Kanatzidis, J. Am. Chem. Soc. 137 (24) (2015) 7843–7850.
- [55] C.R. Kagan, D.B. Mitzi, C.D. Dimitrakopoulos, Science 286 (5441) (1999) 945–947.

- [56] Z. Xiao, W. Meng, B. Saparov, H.-S. Duan, C. Wang, C. Feng, W. Liao, W. Ke, D. Zhao, J. Wang, D.B. Mitzi, Y. Yan, J. Phys. Chem. Lett. 7 (2016) 1213–1218.
- [57] D. Umeyama, Y. Lin, H.I. Karunadasa, Chem. Mater. 28 (2016) 3241-3244.
- [58] Y. Zhao, K. Zhu, J. Am. Chem. Soc. 136 (35) (2014) 12241–12244.
- [59] L. Kong, G. Liu, J. Gong, Q. Hu, R.D. Schaller, P. Dera, D. Zhang, Z. Liu, W. Yang, K. Zhu, Y. Tang, C. Wang, S.-H. Wei, T. Xu, H.-k. Mao, Proc. Natl. Acad. Sci. USA 113 (32) (2016) 8910-8915.
- [60] C.C. Stoumpos, C.D. Malliakas, M.G. Kanatzidis, Inorg. Chem. 52 (15) (2013) 9019-9038.
- [61] A. Swarnkar, A.R. Marshall, R.M. Sanehira, B.D. Chernomordik, D.T. Moore, J.A. Christians, T. Chakrabarti, J.M. Luther, Science 354 (6308) (2016) 92-95.
- [62] S. Dastidar, C.J. Hawley, A.D. Dillon, A.D. Gutierrez-Perez, J.E. Spanier, A.T. Fafarman, J. Phys. Chem. Lett. 8 (2017) 1278-1282.
- [63] Z. Li, M. Yang, J.-S. Park, S.-H. Wei, J.J. Berry, K. Zhu, Chem. Mater. 28 (1) (2016) 284-292.
- [64] L. Protesescu, S. Yakunin, M.I. Bodnarchuk, F. Krieg, R. Caputo, C.H. Hendon, R.X. Yang, A. Walsh, M.V. Kovalenko, Nano Lett. 15 (2015) 3692-3696.
- [65] G.E. Eperon, G.M. Paterno, R.J. Sutton, A. Zampetti, A.A. Haghighirad, F. Ca-
- cialli, H.J. Snaith, J. Mater. Chem. A 3 (2015) 19688-19695. [66] W.S. Yang, J.H. Noh, N.J. Jeon, Y.C. Kim, S. Ryu, J. Seo, S.I. Seok, Science 348
- (6240) (2015) 1234-1237. [67] G. Liu, L. Kong, J. Gong, W. Yang, H.-k. Mao, Q. Hu, Z. Liu, R.D. Schaller,
- D. Zhang, T. Xu, Adv. Funct. Mater. 27 (3) (2017) 1604208. [68] M.I. Saidaminov, A.L. Abdelhady, G. Maculan, O.M. Bakr, Chem. Commun. 51
- (2015) 17658-17661. [69] N.J. Jeon, J.H. Noh, W.S. Yang, Y.C. Kim, S. Ryu, J. Seo, S.I. Seok, Nature 517
- (2015) 476-480. [70] N. Pellet, P. Gao, G. Gregori, T.-Y. Yang, M.K. Nazeeruddin, J. Maier, M. Gratzel,
- Angew. Chem. Int. Ed. 53 (12) (2014) 3151-3157. [71] G.E. Eperon, S.D. Stranks, C. Menelaou, M.B. Johnston, L.M. Herz, H.J. Snaith,
- Energy Environ. Sci. 7 (2014) 982-988. [72] Q. Han, S.-H. Bae, P. Sun, Y.-T. Hsieh, Y.M. Yang, Y.S. Rim, H. Zhao, Q. Chen,
- W. Shi, G. Li, Y. Yang, Adv. Mater. 28 (2016) 2253-2258.
- [73] M.T. Weller, O.J. Weber, J.M. Frost, A. Walsh, J. Phys. Chem. Lett. 6 (16) (2015) 3209-3212.
- [74] A.A. Zhumekenov, M.I. Saidaminov, M.A. Haque, E. Alarousu, S.P. Sarmah, B. Murali, I. Dursun, X.-H. Miao, A.L. Abdelhady, T. Wu, O.F. Mohammed, O.M. Bakr, ACS Energy Lett. 1 (1) (2016) 32-37.
- [75] Z. Zhou, S. Pang, F. Ji, B. Zhang, G. Cui, Chem. Commun. 52 (2016) 3828–3831.
- [76] A. Amat, E. Mosconi, E. Ronca, C. Quarti, P. Umari, M.K. Nazeeruddin, M. Gratzel, F. De Angelis, Nano Lett. 14 (6) (2014) 3608-3616.
- [77] W. Travis, E.N.K. Glover, H. Bronstein, D.O. Scanlon, R.G. Palgrave, Chem. Sci. 7 (2016) 4548-4556
- [78] H. Tan, A. Jain, O. Voznyy, X. Lan, F.P.G. de Arquer, J.Z. Fan, R. Quintero-Bermudez, M. Yuan, B. Zhang, Y. Zhao, F. Fan, P. Li, L.N. Quan, Y. Zhao, Z.-H. Lu, Z. Yang, S. Hoogland, E.H. Sargent, Science 355 (6326) (2017) 722-726.
- [79] M. Liu, M.B. Johnston, H.J. Snaith, Nature 501 (2013) 395-398.
- [80] M.A. Loi, J.C. Hummelen, Nat. Mater. 12 (2013) 1087-1089.
- [81] W. Zhang, M. Saliba, D.T. Moore, S.K. Pathak, M.T. Horantner, T. Stergiopoulos, S.D. Stranks, G.E. Eperon, J.A. Alexander-Webber, A. Abate, A. Sadhanala, S. Yao, Y. Chen, R.H. Friend, L.A. Estroff, U. Wiesner, H.J. Snaith, Nat. Commun. 6 (2015) 6142.
- [82] Q. Chen, H. Zhou, Z. Hong, S. Luo, H.-S. Duan, H.-H. Wang, Y. Liu, G. Li, Y. Yang, J. Am. Chem. Soc. 136 (2) (2014) 622-625.
- [83] S. Bai, N. Sakai, W. Zhang, Z. Wang, J.T.-W. Wang, F. Gao, H.J. Snaith, Chem. Mater. 29 (1) (2017) 462–473.
- B. Wang, K.Y. Wong, X. Xiao, T. Chen, Sci. Rep. 5 (2015) 10557
- [85] M.M. Tavakoli, L. Gu, Y. Gao, C. Reckmeier, J. He, A.L. Rogach, Y. Yao, Z. Fan, Sci. Rep. 5 (2015) 14083.
- [86] E.M. Sanehira, B.J.T. de Villers, P. Schulz, M.O. Reese, S. Ferrere, K. Zhu, L.Y. Lin, J.J. Berry, J.M. Luther, ACS Energy Lett. 1 (1) (2016) 38-45.
- [87] Y. Zhao, A.M. Nardes, K. Zhu, Appl. Phys. Lett. 104 (2014) 213906
- [88] J. Meyer, S. Hamwi, M. Kroger, W. Kowalsky, T. Riedl, A. Kahn, Adv. Mater. 24 40) (2012) 5408-5427.
- [89] P. Schulz, J.O. Tiepelt, J.A. Christians, I. Levine, E. Edri, E.M. Sanehira, G. Hodes, D. Cahen, A. Kahn, ACS Appl. Mater. Interfaces 8 (46) (2016) 31491-31499.
- [90] Q. Wang, X. Zheng, Y. Deng, J. Zhao, Z. Chen, J. Huang, Joule 1 (2) (2017) 371-382.
- [91] E.M. Sanehira, A.R. Marshall, J.A. Christians, S.P. Harvey, P.N. Ciesielski, L.M. Wheeler, P. Schulz, L.Y. Lin, M.C. Beard, J.M. Luther, Sci. Adv. 3 (10) (2017), doi:10.1126/sciadv.aao4204.
- [92] R.J. Sutton, G.E. Eperon, L. Miranda, E.S. Parrott, B.A. Kamino, J.B. Patel, M.T. Horantner, M.B. Johnston, A.A. Haghighirad, D.T. Moore, H.J. Snaith, Adv. Energy Mater. 6 (8) (2016) 1502458.
- [93] J. You, Y.M. Yang, Z. Hong, T.-B. Song, L. Meng, Y. Liu, C. Jiang, H. Zhou, W.-H. Chang, G. Li, Y. Yang, Appl. Phys. Lett. 105 (2014) 183902.
- [94] Z. Xiao, C. Bi, Y. Shao, Q. Dong, Q. Wang, Y. Yuan, C. Wang, Y. Gao, J. Huang, Energy Environ. Sci. 7 (2014) 2619-2623.
- [95] I. Chung, J.-H. Song, J. Im, J. Androulakis, C.D. Malliakas, H. Li, A.J. Freeman, J.T. Kenney, M.G. Kanatzidis, J. Am. Chem. Soc. 134 (20) (2012) 8579-8587
- [96] S. Hirotsu, J. Harada, M. Lizumi, K. Gesi, J. Phys. Soc. Jpn. 37 (5) (1974) 1393-1398.
- [97] C.C. Stoumpos, C.D. Malliakas, J.A. Peters, Z. Liu, M. Sebastian, J. Im, T.C. Chasapis, A.C. Wibowo, D.Y. Chung, A.J. Freeman, B.W. Wessels, M.G. Kanatzidis, Cryst. Growth Des. 13 (7) (2013) 2722-2727.

- [98] Y. Fu, M.T. Rea, J. Chen, D.J. Morrow, M.P. Hautzinger, Y. Zhao, D. Pan, L.H. Manger, J.C. Wright, R.H. Goldsmith, S. Jin, Chem. Mater. 29 (19) (2017) 8385-8394.
- [99] P. Guo, Y. Xia, J. Gong, C.C. Stoumpos, K.M. McCall, G.C.B. Alexander, Z. Ma, H. Zhou, D.J. Gosztola, J.B. Ketterson, M.G. Kanatzidis, T. Xu, M.K.Y. Chan, R.D. Schaller, ACS Energy Lett. 2 (10) (2017) 2463-2469.
- [100] A. Binek, F.C. Hanusch, P. Docampo, T. Bein, J. Phys. Chem. Lett. 6 (7) (2015) 1249-1253.
- [101] Y. Fu, T. Wu, J. Wang, J. Zhai, M.J. Shearer, Y. Zhao, R.J. Hamers, E. Kan,
- K. Deng, X.-Y. Zhu, S. Jin, Nano Lett. 17 (7) (2017) 4405–4414. [102] Y. Fu, H. Zhu, A.W. Schrader, D. Liang, Q. Ding, P. Joshi, L. Hwang, X.-Y. Zhu, S. Jin, Nano Lett. 16 (2) (2016) 1000-1008.
- [103] J.-W. Lee, D.-J. Seol, A.-N. Cho, N.-G. Park, Adv. Mater. 26 (29) (2014) 4991-4998.
- [104] J. Kim, J.S. Yun, X. Wen, A.M. Soufiani, C.F.J. Lau, B. Wilkinson, J. Seidel, M.A. Green, S. Huang, A.W.Y. Ho-Baillie, J. Phys. Chem. C 120 (20) (2016) 11262-11267.
- [105] J.-W. Lee, S.H. Lee, H.-S. Ko, J. Kwon, J.H. Park, S.M. Kang, N. Ahn, M. Choi, J.K. Kim, N.-G. Park, J. Mater. Chem. A 3 (2015) 9179-9186
- [106] J. Xi, Z. Wu, K. Xi, H. Dong, B. Xia, T. Lei, F. Yuan, W. Wu, B. Jiao, X. Hou, Nano Energy 26 (2016) 438-445.
- [107] S. Pang, H. Hu, J. Zhang, S. Lv, Y. Yu, F. Wei, T. Qin, H. Xu, Z. Liu, G. Cui, Chem. Mater. 26 (3) (2014) 1485-1491.
- [108] C. Wu, X. Zheng, Q. Yang, Y. Yan, M. Sanghadasa, S. Priya, J. Phys. Chem. C 120 (47) (2016) 26710-26719.
- [109] F. Wang, H. Yu, H. Xu, N. Zhao, Adv. Funct. Mater. 25 (7) (2015) 1120-1126
- [110] Y. Zhang, J. Wang, J. Xu, W. Chen, D. Zhu, W. Zheng, X. Bao, RSC Adv. 6 (2016) 79952-79957
- [111] L.Q. Fan, J.H. Wu, Acta Crystallogr. E63 (2007) i189.
- [112] H.J. Snaith, A. Abate, J.M. Ball, G.E. Eperon, T. Leijtens, N.K. Noel, S.D. Stranks, J.T.-W. Wang, K. Wojciechowski, W. Zhang, J. Phys. Chem. Lett. 5 (2014) 1511-1515.
- [113] Y. Wu, A. Islam, X. Yang, C. Qin, J. Liu, K. Zhang, W. Peng, L. Han, Energy Environ. Sci. 7 (2014) 2934-2938.
- [114] S. Mabrouk, A. Dubey, W. Zhang, N. Adhikari, B. Bahrami, M.N. Hasan, S. Yang, Q. Qiao, J. Phys. Chem. C 120 (43) (2016) 24577-24582.
- [115] D.V. Shinde, L. Pyeon, M. Pei, G.-W. Kim, H. Yang, T. Park, ACS Appl. Mater. Interfaces 9 (16) (2017) 14023-14030.
- [116] P.-H. Huang, Y.-H. Wang, J.-C. Ke, C.-J. Huang, Energies 10 (5) (2017) 599.
- [117] D. Cui, Z. Yang, D. Yang, X. Ren, Y. Liu, Q. Wei, H. Fan, J. Zeng, S.F. Liu, J. Phys. Chem. C 120 (1) (2016) 42-47.
- [118] I. Karimata, Y. Kobori, T. Tachikawa, J. Phys. Chem. Lett. 8 (8) (2017) 1724-1728.
- [119] P.F. Ndione, Z. Li, K. Zhu, J. Mater. Chem. C 4 (2016) 7775-7782.
- [120] R.E. Beal, D.J. Slotcavage, T. Leijtens, A.R. Bowring, R.A. Belisle, W.H. Nguyen, G.F. Burkhard, E.T. Hoke, M.D. McGehee, J. Phys. Chem. Lett. 7 (5) (2016) 746-751.
- [121] P. Luo, W. Xia, S. Zhou, L. Sun, J. Cheng, C. Xu, Y. Lu, J. Phys. Chem. Lett. 7 (18) (2016) 3603-3608.
- [122] X. Chang, W. Li, L. Zhu, H. Liu, H. Geng, S. Xiang, J. Liu, H. Chen, ACS Appl. Mater. Interfaces 8 (49) (2016) 33649-33655
- [123] M. Kulbak, S. Gupta, N. Kedem, Levine I, T. Bendikov, G. Hodes, D. Cahen, J. Phys. Chem. Lett. 7 (1) (2016) 167-172.
- [124] M.I. Saidaminov, A.L. Abdelhady, B. Murali, E. Alarousu, V.M. Burlakov, W. Peng, I. Dursun, L. Wang, Y. He, G. Maculan, A. Goriely, T. Wu, O.F. Mohammed, O.M. Bakr, Nat. Commun. 6 (2015) 7586.
- [125] Y. Rakita, N. Kedem, S. Gupta, A. Sadhanala, V. Kalchenko, M.L. Bohm, M. Kulbak, R.H. Friend, D. Cahen, G. Hodes, Cryst. Growth Des. 16 (10) (2016) 5717-5725.
- [126] F. Deschler, M. Price, S. Pathak, L.E. Klintberg, D.-D. Jarausch, R. Higler, S. Huttner, T. Leijtens, S.D. Stranks, H.J. Snaith, M. Atature, R.T. Phillips, R.H. Friend, J. Phys. Chem. Lett. 5 (8) (2014) 1421-1426.
- [127] G. Niu, W. Li, J. Li, X. Liang, L. Wang, RSC Adv. 7 (2017) 17473-17479.
- [128] J. Dai, Y. Fu, L.H. Manger, M.T. Rea, L. Hwang, R.H. Goldsmith, S. Jin, J. Phys. Chem. Lett. 7 (2016) 5036-5043.
- [129] Y. Zhang, G. Grancini, Y. Feng, A.M. Asiri, M.K. Nazeeruddin, ACS Energy Lett. 2 (4) (2017) 802–806.
- [130] M. Saliba, T. Matsui, K. Domanski, J.-Y. Seo, A. Ummadisingu, S.M. Zakeeruddin, J.-P. Correa-Baena, W.R. Tress, A. Abate, A. Hagfeldt, M. Gratzel, Science 354 (6309) (2016) 206-209.
- [131] M. Saliba, T. Matsui, J.-Y. Seo, K. Domanski, J.-P. Correa-Baena, M.K. Nazeeruddin, S.M. Zakeeruddin, W. Tress, A. Abate, A. Hagfeldt, M. Gratzel, Energy Environ. Sci. 9 (2016) 1989-1997.
- [132] X. Zheng, C. Wu, S.K. Jha, Z. Li, K. Zhu, S. Priya, ACS Energy Lett. 1 (5) (2016) 1014-1020.
- [133] D. Bi, W. Tress, M.I. Dar, P. Gao, J. Luo, C. Renevier, K. Schenk, A. Abate, F. Giordano, J.-P.C. Baena, J.-D. Decoppet, S.M. Zakeeruddin, M.K. Nazeeruddin, M. Gratzel, A. Hagfeldt, Sci. Adv. 2 (1) (2016) e1501170.
- [134] J.-P. Correa-Baena, M. Anaya, G. Lozano, W. Tress, K. Domanski, M. Saliba, T. Matsui, T.J. Jacobsson, M.E. Calvo, A. Abate, M. Gratzel, H. Miguez, A. Hagfeldt, Adv. Mater. 28 (25) (2016) 5031-5037.
- [135] M. Gratzel, Acc. Chem. Res. 50 (3) (2017) 487-491.
- [136] Z.-K. Tan, R.S. Moghaddam, M.L. Lai, P. Docampo, R. Higler, F. Deschler, M. Price, A. Sadhanala, L.M. Pazos, D. Credgington, F. Hanusch, T. Bein, H.J. Snaith, R.H. Friend, Nat. Nanotechnol. 9 (2014) 687-692.

JID: JECHEM ARTICLE IN PRESS [m5G;January 11, 2018;19:0]

J. Gong et al./Journal of Energy Chemistry 000 (2018) 1-23

- [137] J. Xing, F. Yan, Y. Zhao, S. Chen, H. Yu, Q. Zhang, R. Zeng, H.V. Demir, X. Sun, A. Huan, Q. Xiong, ACS Nano. 10 (7) (2016) 6623–6630.
- [138] S.D. Stranks, H.J. Snaith, Nat. Nanotechnol. 10 (2015) 391-402
- [139] Y.-H. Kim, H. Cho, J.H. Heo, T.-S. Kim, N. Myoung, C.-L. Lee, S.H. Im, T.-W. Lee, Adv. Mater. 27 (7) (2015) 1248–1254.
- [140] S.A. Veldhuis, P.P. Boix, N. Yantara, M. Li, T.C. Sum, N. Mathews, S.G. Mhaisalkar, Adv. Mater. 28 (32) (2016) 6804–6834.
- [141] H. Cho, S.-H. Jeong, M.-H. Park, Y.-H. Kim, C. Wolf, C.-L. Lee, J.H. Heo, A. Sadhanala, N. Myoung, S. Yoo, S.H. Im, R.H. Friend, T.-W. Lee, Science 350 (6265) (2015) 1222–1225.
- [142] L. Gil-Escrig, G. Longo, A. Pertegas, C. Roldan-Carmona, A. Soriano, M. Sessolo, H.J. Bolink, Chem. Commun. 51 (2015) 569–571.
- [143] G. Li, F.W.R. Rivarola, N.J.L.K. Davis, S. Bai, T.C. Jellicoe, F. de la Pena, S. Hou, C. Ducati, F. Gao, R.H. Friend, N.C. Greenham, Z.-K. Tan, Adv. Mater. 28 (18) (2016) 3528–3534.
- [144] L.K. Ono, E.J. Juarez-Perez, Y. Qi, ACS Appl. Mater. Interfaces 9 (36) (2017) 30197–30246.
- [145] Y.H. Park, I. Jeong, S. Bae, H.J. Son, P. Lee, J. Lee, C.-H. Lee, M.J. Ko, Adv. Funct. Mater. 27 (16) (2017) 1605988.
- [146] Y. Hu, M.F. Ayguler, M.L. Petrus, T. Bein, P. Docampo, ACS Energy Lett. 2 (10) (2017) 2212–2218.
- [147] Q. Jiang, M. Chen, J. Li, M. Wang, X. Zeng, T. Besara, J. Lu, Y. Xin, X. Shan, B. Pan, C. Wang, S. Lin, T. Siegrist, Q. Xiao, Z. Yu, ACS Nano 11 (1) (2017) 1073–1079.
- [148] G. Giorgi, J.-I. Fujisawa, H. Segawa, K. Yamashita, J. Phys. Chem. C 119 (2015) 4694–4701.
- [149] G. Kieslich, S. Sun, A.K. Cheetham, Chem. Sci. 5 (2014) 4712-4715.
- [150] N. De Marco, H. Zhou, Q. Chen, P. Sun, Z. Liu, L. Meng, E.-P. Yao, Y. Liu, A. Schiffer, Y. Yang, Nano Lett. 16 (2016) 1009–1016.
- [151] R.D. Shannon, Acta Cryst. A32 (1976) 751-767.
- [152] L. Dimesso, A. Quintilla, Y.-M. Kim, U. Lemmer, W. Jaegermann, Mater. Sci. Eng. B 204 (2016) 27–33.
- [153] C.C. Stoumpos, D.H. Cao, D.J. Clark, J. Young, J.M. Rondinelli, J.I. Jang, J.T. Hupp, M.G. Kanatzidis, Chem. Mater. 28 (8) (2016) 2852–2867.
- [154] M. Shimizu, J.-I. Fujisawa, J. Ishi-Hayase, Phys. Rev. B 71 (2005) 205306.
- [155] K. Tanaka, T. Takahashi, T. Kondo, T. Umebayashi, K. Asai, K. Ema, Phys. Rev. B 71 (2005) 045312.
- [156] I.B. Koutselas, L. Ducasse, G.C. Papavassiliou, J. Phys.: Condens. Matter 8 (9) (1996) 1217–1227.
- [157] K. Tanaka, T. Kondo, Sci. Technol. Adv. Mater. 4 (6) (2003) 599-604.
- [158] G. Liu, L. Kong, P. Guo, C.C. Stoumpos, Q. Hu, Z. Liu, Z. Cai, D.J. Gosztola, H.-k. Mao, M.G. Kanatzidis, R.D. Schaller, ACS Energy Lett. 2 (2017) 2518–2524.

- [159] K. Yao, X. Wang, F. Li, L. Zhou, Chem. Commun. 51 (2015) 15430-15433.
- [160] K. Yao, X. Wang, Y.-x. Xu, F. Li, L. Zhou, Chem. Mater. 28 (9) (2016) 3131–3138.
- [161] P.P. Boix, S. Agarwala, T.M. Koh, N. Mathews, S.G. Mhaisalkar, J. Phys. Chem. Lett. 6 (5) (2015) 898–907.
- [162] X. Gan, O. Wang, K. Liu, X. Du, L. Guo, H. Liu, Sol. Energy Mater. Sol. Cells 162 (2017) 93–102.
- [163] M.C. Beard, J.M. Luther, A.J. Nozik, Nat. Nanotechnol. 9 (2014) 951–954.
- [164] E. Zimmermann, P. Ehrenreich, T. Pfadler, J.A. Dorman, J. Weickert, L. Schmidt-Mende, Nat. Photon. 8 (2014) 669–672.
- [165] K.D.G.I. Jayawardena, L.J. Rozanski, C.A. Mills, S.R.P. Silva, Nat. Photon. 9 (2015) 207–208.
- [166] Nat. Nanotech. 9 (2014) 657. doi:10.1038/nnano.2014.206.
- [167] C.-J. Tong, W. Geng, O.V. Prezhdo, L.-M. Liu, ACS Energy Lett. 2 (2017) 1997–2004.
- [168] Y. Fu, H. Zhu, C.C. Stoumpos, Q. Ding, J. Wang, M.G. Kanatzidis, X. Zhu, S. Jin, ACS Nano 10 (8) (2016) 7963–7972.
- [169] H. Zhu, Y. Fu, F. Meng, X. Wu, Z. Gong, Q. Ding, M.V. Gustafsson, M.T. Trinh, S. Jin, X-Y. Zhu, Nat. Mater. 14 (2015) 636–642.
- [170] Y. Fu, F. Meng, M.B. Rowley, B.J. Thompson, M.J. Shearer, D. Ma, R.J. Hamers, J.C. Wright, S. Jin, J. Am. Chem. Soc. 137 (17) (2015) 5810–5818.
- [171] D. Zhang, S.W. Eaton, Y. Yu, L. Dou, P. Yang, J. Am. Chem. Soc. 137 (29) (2015) 9230–9233.
- [172] L. Dou, Y.M. Yang, J. You, Z. Hong, W.-H. Chang, G. Li, Y. Yang, Nat. Commun. 5 (2014) 5404.
- [173] G. Xing, N. Mathews, S.S. Lim, N. Yantara, X. Liu, D. Sabba, M. Gratzel, S. Mhaisalkar, T.C. Sum, Nat. Mater. 13 (2014) 476–480.
- [174] J. Ding, S. Du, Y. Zhao, X. Zhang, Z. Zuo, H. Cui, X. Zhan, Y. Gu, H. Sun, J. Mater.
- Sci. 52 (1) (2017) 276–284. [175] Z. Lian, Q. Yan, Q. Lv, Y. Wang, L. Liu, L. Zhang, S. Pan, Q. Li, L. Wang, J.-L. Sun,
- Sci. Rep. 5 (2015) 16563. [176] P. Zhu, S. Gu, X. Shen, N. Xu, Y. Tan, S. Zhuang, Y. Deng, Z. Lu, Z. Wang, J. Zhu,
- Nano Lett. 16 (2) (2016) 871–876. [177] B.R. Sutherland, S. Hoogland, M.M. Adachi, C.T.O. Wong, E.H. Sargent, ACS
- Nano 8 (10) (2014) 10947–10952. [178] D. Zhang, Y. Yang, Y. Bekenstein, Y. Yu, N.A. Gibson, A.B. Wong, S.W. Eaton,
- [178] D. Zhang, Y. Yang, Y. Bekenstein, Y. Yu, N.A. Gibson, A.B. Wong, S.W. Eaton, N. Kornienko, Q. Kong, M. Lai, A.P. Alivisatos, S.R. Leone, P. Yang, J. Am. Chem. Soc. 138 (23) (2016) 7236–7239.
- [179] L. Dou, M. Lai, C.S. Kley, Y. Yang, C.G. Bischak, D. Zhang, S.W. Eaton, N.S. Ginsberg, P. Yang, Proc. Natl. Acad. Sci. USA 114 (28) (2017) 7216–7221.

23